Author/s:
Monfared, O;Tahayori, B;Freestone, D;Nesic, D;Grayden, DB;Meffin, H

Title:
Determination of the electrical impedance of neural tissue from its microscopic cellular constituents

Date:
2020-02-01

Citation:
Monfared, O., Tahayori, B., Freestone, D., Nesic, D., Grayden, D. B. & Meffin, H. (2020). Determination of the electrical impedance of neural tissue from its microscopic cellular constituents. Journal of Neural Engineering, 17 (1), https://doi.org/10.1088/1741-2552/ab560a.

Determination of the Electrical Impedance of Neural Tissue from its Microscopic Cellular Constituents

Omid Monfared[1,2], Bahman Tahayori[2], Dean Freestone[3], Dragan Nesic[1], David B. Grayden[2,4], and Hamish Meffin [5,6]
[1] *Department of Electrical and Electronic Engineering, The University of Melbourne, Australia*
[2] *Department of Biomedical Engineering, The University of Melbourne, Australia*
[3] *Department of Medicine, The University of Melbourne, Australia*
[4] *Centre for Neural Engineering, The University of Melbourne, Australia*
[5] *Department of Optometry and Vision Sciences, The University of Melbourne, Australia*
[6] *National Vision Research Institute, Australian College of Optometry, Australia*
(Dated: November 4, 2019)

The electrical properties of neural tissue are important in a range of different applications in biomedical engineering and basic science. These properties are characterized by the electrical admittivity of the tissue, which is the inverse of the specific tissue impedance. Here we derived analytical expressions for the admittivity of various models of neural tissue from the underlying electrical and morphological properties of the constituent cells. Three models are considered: parallel bundles of fibers, fibers contained in stacked laminae and fibers crossing each other randomly in all three-dimensional directions. An important and novel aspect that emerges from considering the underlying cellular composition of the tissue is that the resulting admittivity has both spatial and temporal frequency dependence, a property not shared with conventional conductivity-based descriptions. The frequency dependence of the admittivity results in non-trivial spatiotemporal filtering of electrical signals in the tissue models. These effects are illustrated by considering the example of pulsatile stimulation with a point source electrode. It is shown how changing temporal parameters of a current pulse, such as pulse duration, alters the spatial profile of the extracellular potential. In a second example, it is shown how the degree of electrical anisotropy can change as a function of the distance from the electrode, despite the underlying structurally homogeneity of the tissue. These effects are discussed in terms of different current pathways through the intra- and extra-cellular spaces, and how these relate to near- and far-field limits for the admittivity (which reduce to descriptions in terms of a simple conductivity). The results highlight the complexity of the electrical properties of neural tissue and provide mathematical methods to model this complexity.

I. INTRODUCTION

Knowledge of electrical properties of neural tissue, such as conductivity, is important in various applications such as therapeutic electrical stimulation of the nervous system [1–5], electrical impedance tomography (EIT) [6], and interpretation of intrinsic electrical signals in neuroscience [7–9]. A good model of electrical stimulation improves our understanding of electrical stimulation parameters and their effect on tissue response.

It is usually assumed that neural tissue can be described by a locally homogeneous conductivity or resistivity that captures the bulk properties of heterogeneous cellular microstructure. However, the cellular structure of tissue creates a complex partition of intra- and extracellular spaces that are separated by a high-impedance membrane. In neural tissue, the length scales that characterize different aspects of this microstructure vary over many orders of magnitude. Neural tissue contains fibers that are thin but long, in the order of a micron wide but hundreds to thousands of micrometers in length. Furthermore, these fibers are tightly packed in neural tissue, so that the extracellular space is very confined, around 50 nanometers in width [10, 11]. The assumption underlying the characterization of tissue electrical properties by a simple electrical conductivity is that these microstructural inhomogeneities can be averaged out over some length scale. However, when the averaging is done carefully via a mean-field approach, it has been shown this is not the case due to the complicated paths taken by current through the tissue that pass between extra- and intracellular spaces over a range of different length scales [12, 13].

Intuitively, this is depicted schematically in Fig. 1, where the intracellular space is shown in gray. The fibers are separated by a thin extracellular space shown in blue, which has high effective specific resistance due to its small cross-section. Close to the electrode, current is forced to pass through this confined extracellular space because the membrane impedance is very high. However, given sufficient length of passage along the fiber, most of the current in that direction can gradually pass through the membrane to access the intracellular pathway, which has a larger cross-section and lower effective specific resistance compared to the extracellular space. This current redistribution occurs over spatial scales dictated by the electrotonic length constant of the neural fiber [14]. The length constant determines the spatial extent over which a perturbation in the membrane potential of a neurite by a point source stimulus can propagate to affect other sections [15]. Therefore, the effective conductivity changes as a function of the electrode-neurite separation, from smaller to larger values as separation increases. This effect cannot be captured by a simple tissue conductivity. Furthermore, the membrane of each cell has a capacitive property due to its construction from a highly insulating

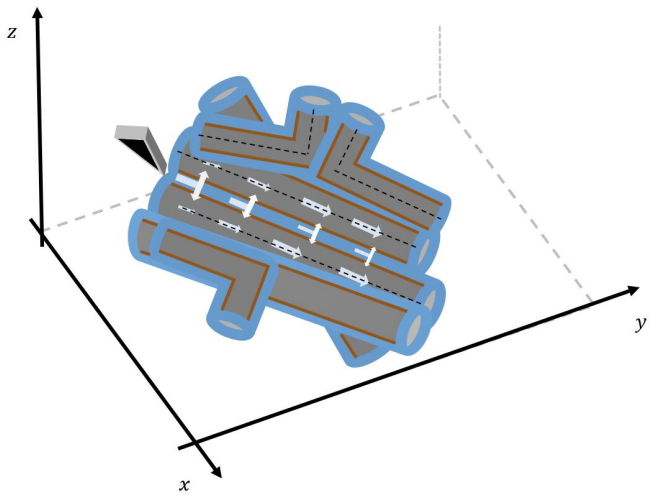

FIG. 1: Schematic illustrating how current passes through neural tissue. Current (white arrows) from an electrode (black triangle) passes through different paths beginning in the extracellular space (blue) and eventually entering the intracellular space (gray) via the neurite membrane (brown). The size of the white arrows indicates the magnitude of the current. The neurites are shown in a quasi-cross-sectional view to allow visualization of the different domains.

phospholipid bilayer, leading to a temporal frequency-dependent impedance between the extracellular and intracellular spaces governed by the membrane time constant.

A modified approach that takes into account the cellular composition of the neural tissue was proposed in [12, 16, 17] which introduced tissue admittivity with spatial and temporal frequency dependence to replace the standard tissue conductivity. Admittivity is the specific admittance of a material, and is the reciprocal of the specific electrical impedance. It is a complex quantity with real part corresponding to the conductivity and the imaginary part corresponding to the susceptibility (here related to the membrane capacitance), with units of Siemens per meter. The aim of the approach was to consider the effect of the cellular composition of tissue, especially the microscale inhomogeneities starting from the underlying biophysics. This was achieved by calculating how the admittivity of tissue arose from the electrical properties of its cellular constituents. This admittivity is an estimation of the bulk electrical properties of neural tissue, derived directly from the impedance of individual neurites and their surrounding thin extracellular sheath [12, 16]. The novel feature of the derived admittivity is that it has both spatial and temporal spectral frequency dependence, which leads to non-trivial spatiotemporal electrical filtering properties of neural tissue. While the idea that the admittivity of a substance may exhibit temporal frequency dependence is well understood, the concept of a spatial frequency dependence is novel. Its meaning and implications for electrical signals in the brain are considered further in this paper.

The expression derived previously giving the spatial and temporal frequency dependence of the tissue admittivity applied only to neural tissue with parallel fiber arrangements, such as a fiber bundle [12, 13]. In this study, we obtain expressions for the tissue admittivity of a more general class of neural tissue models that involve fibers crossing with a variety of orientations. This models neural tissue with different cellular morphologies and arrangements of fibers. Examples of these tissues include laminar structures with fibers in stacked two dimensional planes (similar to retinal ganglion cells and amacrine cells in the retina, and apical or basal dendrites of pyramidal cells in the neocortex) and fibers radiating in three-dimensions (similar to stellate cells in neocortex). This considerably broadens the scope of application of the approach to cover many commonly encountered tissues in the nervous system.

We find the range of spatial and temporal frequency dependence of the admittivity is relevant to a wide variety of electrical signals in the brain, both intrinsic and artificially induced, via electrical stimulation with neurostimulators. These signals operate over a range of spatial and temporal frequencies. For clinical neurostimulators, typically biphasic current pulses are employed with durations around 1 ms down to tens of μs (e.g. [18–21]) so that most of the power occurs for temporal frequencies over 1 kHz but under tens of kHz. The intrinsic signals of the brain such as, alpha, beta and gamma band activities, operate in lower temporal frequency ranges, from less than a 1 Hz up to over 100 Hz [22]; while spiking activity is faster with power up to around 1-2 kHz [23, 24]. The spatial frequency range of bionic electrical stimulation has significant power at the size and spacing of electrodes on the stimulating array. This varies widely with different devices, with the densest arrays having around 100 cycles/mm [25, 26]. Intrinsically, brain structures show many different spatial scales including ion channels, synapses, neurons, cortical columns areas, gyri, and lobes that range from nanometers to tens of centimeters scales [23]. Electrical activity in the brain shows variation across a corresponding range of spatial frequencies (10^{-2} to 10^{6} cycles/mm).

To illustrate some of the main novel consequences of having a spatiotemporal frequency-dependent tissue admittivity, we use the example of pulsed (monophasic) point source stimulation. We also show how these consequences can be affected by different fiber arrangements within the tissue. First, we show how a variation in a temporal parameter, namely applied pulse-width, can affect a spatial property like the profile of the extracellular potential. Second, we show that for tissue with a homogeneous structural anisotropy (i.e., the anisotropy does not change with distance from the electrode, such as in a laminar structure) variation in a spatial variable, namely distance from the electrode, can nonetheless affect the

degree of anisotropy in the electrical potential. These effects do not occur with a simpler model of conductivity, but are expected to have implications for the application of therapeutic electrical stimulation to the brain via neural prostheses and for interpreting intrinsic brain signals.

II. METHODS

Conductivity and admittivity are defined in terms of their role in constitutive physical equations linking electric current to potential (e.g. Ohms law). In this section, these type of equations are introduced within the mathematical framework of the standard volume conductor (for conductivity) and the cellular composite model (for frequency dependent admittivity). The cellular composite model is introduced as a mean-field approximation to a more fundamental but complex model consisting of many closely packed, possibly crossing, fibers separated from each other by a thin extracellular space. We then describe the three cellular composite models of fiber orientation considered in this study and use those models to calculate the extracellular potential in the presence of a point source electrode.

A. Fundamental Tissue Model

We begin by describing the fundamental and complex model of neural tissue from which a simpler mean-field approximation can be derived. Conceptually, the model consists of many densely packed and typically crossing neurites with a thin extracellular space separating the membranes of neighboring neurites. Each neurite, together with the thin extracellular sheath (NTES) that surrounds it, is taken as a semi-modular element; collectively the tissue is a composite of NTES elements and the electrical properties of the tissue are determined by some aggregation of the electrical properties of its NTES elements. The geometric model of an example NTES element is shown diagrammatically in Fig. 2. It consists of two concentric, infinitely long tubes, with the inner tube representing the neurite, and the region between the inner and outer tubes, representing the extracellular space. The electrical potential in the intracellular and extracellular spaces are governed by Laplace's equation, as per the standard volume conductor in section II B below, with resistivities ρ_{i} and ρ_{e}, respectively. The neural membrane forming the surface of the inner tube is modeled as an electrically passive leaky integrator, with specific resistance, R_{m} and specific capacitance C_{m}, giving a membrane time constant $\tau_{\mathrm{m}} = R_{\mathrm{m}}C_{\mathrm{m}}$. Conceptually, the outer surfaces of adjoining NTES elements fit together seamlessly, leaving no gaps, such that the total width of the extracellular space is approximately twice the width of an individual sheath. In neural tissue, seamless, tight packing is achieved due to irregular deformations in the shape and spatial course of neurites, so that the precise shape of each NTES element is unique. Abutting NTES elements are coupled through the free passage of current across their shared and irregular shaped outer surfaces; mathematically the current density and electrical potential are continuous across these boundaries.

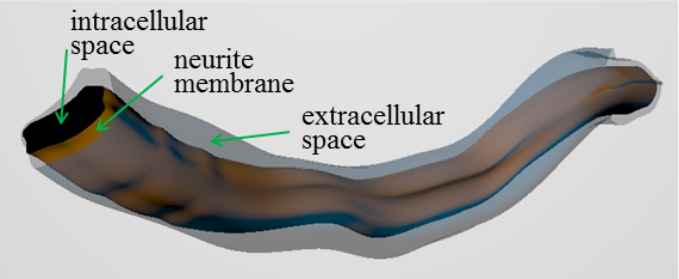

FIG. 2: Schematic showing an example of geometric model element of a neurite plus thin extracellular sheath (NTES) that forms semi-modular elements used to build the model. The neurite membrane is a long thin tube (brown) enclosing an intracellular space (black). The thin extracellular space surrounding the neurite forms a roughly concentric annular tube (blue-gray), which for clarity is drawn with a width several times thicker relative to the neurite width than occurs in biology. In tissue, the NTES element would be packed around tightly with other NTES elements, but is shown here in isolation against a light gray background that is not part of the model.

This model is highly complex due to the complicated, irregular interlocking NTES geometries. As such, it is not amenable to mathematical analysis. In Appendix A we specify the model mathematically and then systematically simplify it to derive a mean-field approximation that takes the form the cellular composite model described in section II C. Broadly, this involves the following steps:

- Replacing the irregularly shaped NTES elements with cylindrical NTES elements with similar proportions and electrical characteristics.
- Replacing the highly complicated coupling between neighboring NTES elements, resulting from their complex, interlocking geometry, with a local mean-field coupling.
- Mathematically simplifying the model and neglecting fluctuations in the electrical potential that occur on spatial scales finer than around 10 neurite diameters.

B. Standard Volume Conductor Model

In the standard volume conductor approach [27, 28], neural tissue is assumed to be purely conductive. The current density, $\mathbf{J}_{\mathrm{e}}$, and the extracellular potential, V_{e},

TABLE I: Fourier transform notations

1D spatial Fourier transform in z:	$\acute{f}(x,y,k_z,t)$
2D spatial Fourier transform in (x,y):	$\hat{f}(k_x,k_y,z,t)$
3D spatial Fourier transform in (x,y,z):	$\check{f}(k_x,k_y,k_z,t)$
Temporal Fourier transform:	$\hat{f}(x,y,z,w)$

are related via the set of equations

$$\begin{aligned} \mathbf{J}_\mathrm{e} &= -\sigma \boldsymbol{\nabla} V_\mathrm{e}, \\ \boldsymbol{\nabla}\cdot\mathbf{J}_\mathrm{e} &= j_\mathrm{e}, \end{aligned} \tag{1}$$

where σ is the constant conductivity of the tissue, $\boldsymbol{\nabla}$ is the three-dimensional spatial gradient operator, $\boldsymbol{\nabla}\cdot$ is the corresponding divergence and j_e is the volumetric current density. The first equation is the constitutive equation defining the conductivity as the constant of proportionality between the current density and the electric fields. The second equation stipulates conservation of current: the volumetric current density j_e is generally zero, indicated conservation of circulating current at all points excepted at current sources or sinks, such as electrodes where it is non-zero. More generally, when tissue is anisotropic, $\boldsymbol{\sigma}$ can be considered a 3×3 symmetric matrix that describes the conductivities in different directions $[x,y,z]$,

$$\boldsymbol{\sigma} = \begin{bmatrix} \sigma_{xx} & \sigma_{xy} & \sigma_{xz} \\ \sigma_{xy} & \sigma_{yy} & \sigma_{yz} \\ \sigma_{xz} & \sigma_{yz} & \sigma_{zz} \end{bmatrix}. \tag{2}$$

While it is possible to have non-zero off-diagonal terms related to conductivity in oblique directions, it is always possible to choose the axis directions to eliminate these so that $\boldsymbol{\sigma}$ is diagonal with conductivities $[\sigma_x,\sigma_y,\sigma_z]$ in the $[x,y,z]$ directions,

$$\boldsymbol{\sigma} = \begin{bmatrix} \sigma_x & 0 & 0 \\ 0 & \sigma_y & 0 \\ 0 & 0 & \sigma_z \end{bmatrix}. \tag{3}$$

C. Cellular Composite Model

To account for the effect of the complicated cellular micro-structure of neural tissue on its bulk electrical properties a new mathematical formalism is required that incorporates the effects of membrane capacitance and complicated current paths between the intracellular and extracellular spaces (refer to the Introduction). The generalized cellular composite model of neural tissue does this by replacing the conductivity matrix in equation (1) with a tissue admittivity kernel, $\boldsymbol{\xi}_\mathrm{e}(\mathbf{r},t)$ [12],

$$\begin{aligned} \mathbf{J}_\mathrm{e} &= -\frac{1}{(2\pi)^2}\boldsymbol{\xi}_\mathrm{e} \underset{\mathbf{r},t}{*} \boldsymbol{\nabla} V_\mathrm{e}, \\ \boldsymbol{\nabla}\cdot\mathbf{J}_\mathrm{e} &= j_\mathrm{e}. \end{aligned} \tag{4}$$

The admittivity kernel is also a 3×3 matrix,

$$\boldsymbol{\xi}_\mathrm{e}(\mathbf{r},t) = \begin{bmatrix} \xi_{xx}(\mathbf{r},t) & \xi_{xy}(\mathbf{r},t) & \xi_{xz}(\mathbf{r},t) \\ \xi_{yx}(\mathbf{r},t) & \xi_{yy}(\mathbf{r},t) & \xi_{yz}(\mathbf{r},t) \\ \xi_{zx}(\mathbf{r},t) & \xi_{zy}(\mathbf{r},t) & \xi_{zz}(\mathbf{r},t) \end{bmatrix}, \tag{5}$$

where $\xi_{xx}(\mathbf{r},t)$, $\xi_{xy}(\mathbf{r},t)$, etc are the admittivity kernels corresponding to various directions. The major difference to conductivity is that the admittivity kernel $\boldsymbol{\xi}_\mathrm{e}(\mathbf{r},t)$ has both a spatial argument $\mathbf{r}=(x,y,z)$ and a temporal argument t. These do not describe the variation of a conventional, but inhomogeneous conductivity, over space and time. Rather they are arguments of a spatiotemporal kernel that is applied to the extracellular electric field $\mathbf{E}_\mathrm{e}=-\boldsymbol{\nabla}V_\mathrm{e}$ via convolution instead of multiplication,

$$\begin{aligned} \boldsymbol{\xi}_\mathrm{e} \underset{\mathbf{r},t}{*} \boldsymbol{\nabla} V_\mathrm{e}(\mathbf{r}',t) &= \int_{t'\in\mathbb{R}}\int_{\mathbf{r}\in\mathbb{R}^3} \boldsymbol{\xi}_\mathrm{e}(\mathbf{r}',t') \\ &\quad\times\ \boldsymbol{\nabla} V_\mathrm{e}(\mathbf{r}-\mathbf{r}',t-t')\mathbf{d}\mathbf{r}'dt'. \end{aligned} \tag{6}$$

The convolutional form has been rigorously derived previously [12] in the case of tissue comprising identical, closely packed, parallel fibers. For a more general situation with tissue comprising crossed fibers a partial derivation is provided in Appendix A. In either case the convolution can be understood intuitively as follows. The temporal convolution arises due to the effect of the membrane capacitance which stores charge from the extracellular space so that the dependence of extracellular current density on the extracellular electric field, occurs not just in the current instant but also at previous times. Similarly, the spatial convolution captures the effects of current paths between points in the extracellular space via "hidden" intracellular pathways along fibers; it relates extracellular current density to the extracellular electrical field at distant points via these "hidden" paths. Perhaps the surprising aspect of this description is that there is no need to describe intervening mechanisms of currents, electric fields or potentials in the intracellular space or neural membrane; their combined effect on the extracellular current density is captured through the contributions of the extracellular electric field at points displaced in time and space (see [12] for deeper explanation).

In the spatial and temporal frequency domain equation (4) regains a simple multiplicative form

$$\begin{aligned} \hat{\check{\mathbf{J}}}_\mathrm{e} &= -\hat{\check{\boldsymbol{\xi}}}_\mathrm{e}\check{\boldsymbol{\nabla}}\hat{\check{V}}_\mathrm{e}, \\ \check{\boldsymbol{\nabla}}\cdot\hat{\check{\mathbf{J}}}_\mathrm{e} &= \hat{\check{j}}_\mathrm{e}, \end{aligned} \tag{7}$$

where the accents $\hat{f}(\mathbf{r},\omega)$ and $\check{f}(\mathbf{k},t)$ above any spatiotemporal function $f(\mathbf{r},t)$, represent the temporal and three-dimensional spatial Fourier transforms, respectively (a full description of the Fourier transform notation is in Table I with definitions of the form of the Fourier transform in Table II). Here, $\check{\boldsymbol{\nabla}} = j[k_x,k_y,k_z]$, which is the three-dimensional Fourier transform for the operator $\boldsymbol{\nabla}$. The factor of $1/(2\pi)^2$ in the space-time version of equation (4) is required as a normalization factor by

TABLE II: Fourier transform definition

Signal	FT equation	Inverse FT equation
$f(\mathbf{r})$	$\check{f}(\mathbf{k}) = \frac{1}{(2\pi)^{3/2}} \int f(\mathbf{r}) e^{-j\mathbf{k}\cdot\mathbf{r}} d\mathbf{r}$	$f(\mathbf{r}) = \frac{1}{(2\pi)^{3/2}} \int \check{f}(k) e^{j\mathbf{k}\cdot\mathbf{r}} d\mathbf{k}$
$h(t)$	$\hat{h}(w) = \frac{1}{\sqrt{2\pi}} \int h(t) e^{-jwt} dt$	$h(t) = \frac{1}{\sqrt{2\pi}} \int \hat{h}(w) e^{jwt} dt$

the convolution when using the unitary definition of the Fourier transform, but vanishes in the frequency domain. We will refer to the frequency representation of the tissue admittivity kernel simply as the tissue admittivity, $\hat{\check{\boldsymbol{\xi}}}_{\mathrm{e}}(\mathbf{k}, \omega)$.

For tissue comprising identical, closely packed, parallel fibers oriented in the direction of a unit column vector $\mathbf{u}$, the tissue admittivity has been shown to have the form [12],

$$\hat{\check{\boldsymbol{\xi}}}_{\mathrm{e},\mathbf{u}}(\mathbf{k}, w) = \hat{\check{\xi}}_{\mathrm{e,T}} \mathbf{I}_{3\times 3} + (\hat{\check{\boldsymbol{\xi}}}_{\mathrm{e,L}}(\mathbf{k}, w|\mathbf{u}) - \hat{\check{\xi}}_{\mathrm{e,T}}) \mathbf{u}\mathbf{u}^T, \quad (8)$$

$$\hat{\check{\xi}}_{\mathrm{e,T}} = \zeta_{\mathrm{e,T}} = \frac{d}{b\rho_{\mathrm{e}}}, \quad (9)$$

$$\hat{\check{\xi}}_{\mathrm{e,L}}(\mathbf{k}, w|\mathbf{u}) = \zeta_{\mathrm{e,L}}(\mathbf{k}^T\mathbf{u}, w) = \frac{1}{\rho_{\mathrm{i}}} \frac{1 + jw\tau_m + (\mathbf{k}^T\mathbf{u})^2\lambda_{0J}^2}{1 + jw\tau_m + (\mathbf{k}^T\mathbf{u})^2\lambda_{0V}^2}. \quad (10)$$

This expression was derived from the equations for the impedance of a single neurite surrounded by a thin extracellular sheath (to model the confined extracellular space)[16]. Note that equation (8) describes a matrix in which $\mathbf{I}_{3\times 3}$ is the 3×3 identity matrix, and $\mathbf{u}\mathbf{u}^T$ is an outer product where $\mathbf{u}^T$ defines the transpose vector of $\mathbf{u}$. The scalar quantities, $\hat{\check{\xi}}_{\mathrm{e,T}}$ and $\hat{\check{\xi}}_{\mathrm{e,L}}(\mathbf{k}, \omega|\mathbf{u})$ are the components of the admittivity, $\hat{\check{\boldsymbol{\xi}}}_{\mathrm{e},\mathbf{u}}(\mathbf{k}, \omega)$, that are transverse and longitudinal to the fibers, respectively. $\zeta_{\mathrm{e,T}}$ and $\zeta_{\mathrm{e,L}}$ are abbreviations for the particular functional forms given in equations (9) and (10) in terms of $\mathbf{k}^T\mathbf{u}$ and w, which will be useful later. The expressions capture the essential properties of the fibers such as their orientation, diameter, and membrane properties; τ_m is the membrane time constant, ρ_{e} and ρ_{i} are the extracellular and intracellular resistivities of tissue, respectively, b is the radius of an ideal cylindrical neurite and d is the thickness of the extracellular sheath (equal to half the width of the extracellular space between neighboring cells). λ_{0J} and λ_{0V} are the electrotonic length constants for the cable equation [16] calculated under two different types of boundary condition (to be explained below): current density and voltage boundary conditions, respectively. They can be expressed in terms of the physical parameters of the fibers,

$$\lambda_{0J}^2 = \frac{r_{\mathrm{m}}}{r_{\mathrm{e}} + r_{\mathrm{i}}}, \qquad \lambda_{0V}^2 = \frac{r_{\mathrm{m}}}{r_{\mathrm{i}}}, \quad (11)$$

where $r_{\mathrm{m}} = \frac{R_{\mathrm{m}}}{2\pi b}$ is the membrane's unit length resistance (units Ωm), R_{m} is the membrane's unit area resistance(units $\Omega\mathrm{m}^2$), $r_{\mathrm{e}} \approx \frac{\rho_{\mathrm{e}}}{2\pi bd}$ is the extracellular resistance per unit length, and $r_{\mathrm{i}} \approx \frac{\rho_{\mathrm{i}}}{\pi b^2}$ is the intracellular resistance per unit length (units $\Omega\mathrm{m}^{-1}$).

These length constants are defined through the model of a neurite plus thin extracellular sheath [16] when calculating the effect of electrical stimulation along the neurite axis. The electrotonic length constants give the rate of exponential decay in the spatial impulse response of the membrane potential for a neurite due to an extracellular stimulus. The stimulus can be modeled either as current density or voltage applied on a thin ring circumscribing the neurite at the boundary of the extracellular sheath surrounding a neurite. The two different boundary conditions result in the derivation of two versions of cable equation that have different electrotonic length constants as represented in equation (11). Both expressions for the length constants appear in the literature, but typically only one is given, without clarifying the role of boundary conditions in determining the correct expression. While the existence of two electrotonic length constants may seem counter-intuitive, they can be reconciled if (and only if) the current density and voltage along the boundary are related to each other by the equations for impedance of the neurite plus thin extracellular sheath, as derived in [16]. This is guaranteed by the form of the admittivity given in equations (9) and (10) in conjunction with the constitutive equation (4) for the cellular composite model. These equations match the specific electrical impedance of the tissue to that of cellular constituents from which the tissue is composed (see [16] and [12] for a further discussion).

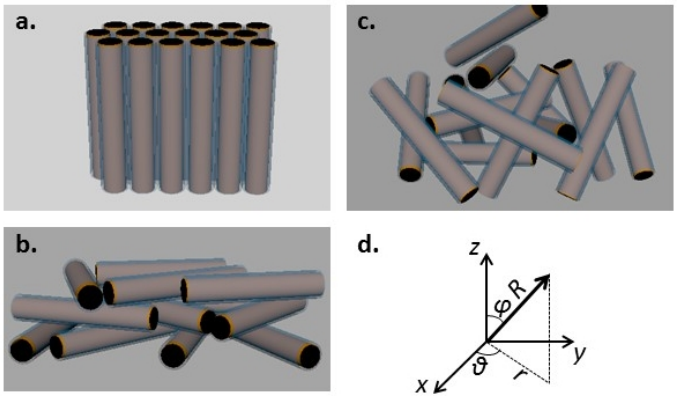

FIG. 3: (a)-(c) Schematics showing arrangement of fibers in the three models considered in this study. (a) Fiber bundle model, with all fibers parallel. (b) Laminar model with fibers confined to a series of stacked planes, but otherwise random in direction (c) Isotropic model, with fibers arranged randomly in all three dimensions. Fibers are assumed to be tightly packed, but this is not shown in the figure for clarity. (d) Schematic showing the cooordinate system used for all three models with alignment with respect to the fibers as it appears in relation to (a)-(c) for the respective models.

D. Three Models of Fiber Orientation Distributions

When tissue is composed of crossing fibers at many orientations, in the direction of unit vectors $\mathbf{u}$, with a probability distribution $P(\mathbf{u})$, the arguments advanced in Appendix A and summarised as dot points at the end of Section II A can be used to show that the current density inside a small volume containing sections from many fibers can be approximated from the mean-field,

$$\hat{\mathbf{J}}_{\rm e} = \int_{|\mathbf{u}|=\mathbf{1}} P(\mathbf{u}) \hat{\mathbf{J}}_{\rm e,\mathbf{u}} d\mathbf{u}, \tag{12}$$

$$\hat{\mathbf{J}}_{\rm e,\mathbf{u}} = -\hat{\boldsymbol{\xi}}_{\rm e,\mathbf{u}} \breve{\boldsymbol{\nabla}} \hat{V}_{\rm e}, \tag{13}$$

where $\hat{\boldsymbol{\xi}}_{\rm e,\mathbf{u}}$ is the admittivity for tissue with fibers in a single direction $\mathbf{u}$. That is, the local (mean-field) current density, $\hat{\mathbf{J}}_{\rm e}$, is the sum of current densities from all fibers, of different orientations, with each seeing the same (mean-field) extracellular potential, $V_{\rm e}$. As the only dependence on $\mathbf{u}$ appears through the admittivity and equations (12) and (13) are linear, the total admittivity of tissue with crossed fibers is given by

$$\boldsymbol{\xi}_{\rm e} = \int_{|\mathbf{u}|=\mathbf{1}} P(\mathbf{u}) \boldsymbol{\xi}_{\rm e,\mathbf{u}} d\mathbf{u}. \tag{14}$$

Here, we consider three different neural tissue models with different distributions of fiber orientation: the fiber bundle model, the laminar tissue model, and the isotropic model (Fig. 3). These correspond to tissue with fibers oriented in one, two, and three dimensions, respectively.

Fiber Bundle Model: As shown in Fig. 3a. this model corresponds to tissue comprising identical, closely packed, parallel fibers as described in the previous subsection. In this case, the orientation vector, $\mathbf{u}$, can be defined trivially as

$$\mathbf{u}^{\rm fb} = [0, 0, 1]^T, \tag{15}$$

assuming that the fiber is oriented along the z-axis.

Laminar Model: As depicted in Fig. 3b., neural tissue is modeled as a stack of xy-planes on top of each other with infinitely long straight fibers uniformly distributed in every direction within each plane. Note that although this arrangement of fibers would in principle result in some fibers intersecting, mathematically we do not allow current to flow directly between the intersecting intracellular spaces. Rather current must always flow between fibers via the extracellular space, just as it occurs in real neural tissue in which fibers twist and bend to pack tightly together in the extracellular space. Details of how this extracellular coupling between fibers is achieved mathematically are given in Appendix A. The orientation vector is defined as

$$\mathbf{u}^{\rm lm} = [\cos\theta, \sin\theta, 0]^T, \tag{16}$$

and the probability density function, $P(\theta)$, is defined to be uniform over the unit circle such that $\int_\theta P(\theta) d\theta = 1$, which means $P(\theta) = 1/2\pi$. This model can serve as an approximation to a variety of tissues with laminar structure, such as the retina that predominantly comprises neurons with planar dendritic morphology.

Isotropic Model: We again assume infinitely long, straight fibers, but with the probability of having fibers in every three-dimensional direction the same. Despite the possibility of intersecting fibers as in the Laminar Model, mathematical coupling between fibers occurs only through extracellular current flow. In the isotropic case, the orientation vector, $\mathbf{u}$, is defined in terms of spherical azimuthal and polar angles, (θ, ϕ),

$$\mathbf{u}^{\rm is} = [\sin\phi\cos\theta, \sin\phi\sin\theta, \cos\phi]^T. \tag{17}$$

This model has a spherically symmetric distribution, $P(\theta, \phi)$, that satisfies the normalization equation, $\int_{\theta,\phi} P(\theta,\phi) d\theta d\phi = 1$, so that $P(\theta, \phi) = \sin\phi/4\pi$. This model can approximate tissue with fibers crossing in all directions, such as when cells have a stellate morphology as shown in Fig. 3c.

The admittivity for each model is reported in the Results, and can be derived by performing the integral in equation (14) over the relevant probability density. This can be done directly, as per equation (14), or (more easily) in the process of solving for the extracellular potential, whereby equation (13) is substituted into equation (12) and hence into the second of equations (7). For the fiber bundle model this was done in [12], for the laminar model this is done in Appendix B and for the isotropic model in [29]. In Appendix C, expressions

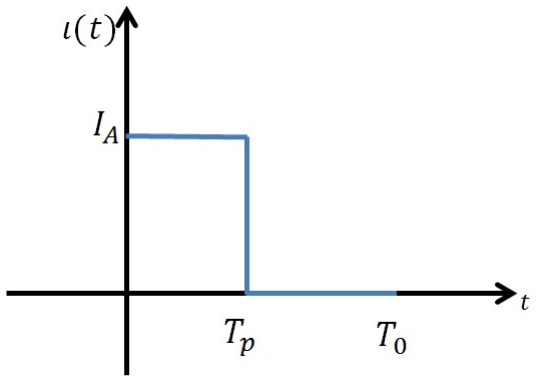

FIG. 4: Monophasic current pulse input with pulse-width of $T_{\rm p}$, period T_0 and amplitude $I_{\rm A}$.

are derived for distributions that have the same type of two- or three-dimensional structure, but can have a more general anisotropic (i.e. nonuniform) distribution of fiber orientation derived from a Gaussian distribution (the spherically projected Gaussian distribution).

E. Solution to Point Source Stimulation

To illustrate some consequences of an admittivity with spatiotemporal frequency dependence, we consider the example of stimulation with a monophasic pulse via a current point source. The effects are reported in the Results but the expressions for extracellular potential of each of the three defined tissue models are derived in the following.

By combining the expressions in equation (4) and adding a point source electrode at the origin, we find

$$\frac{1}{(2\pi)^2}\boldsymbol{\nabla}\cdot\left(\boldsymbol{\xi}_{\rm e}\underset{\mathbf{r},t}{*}\boldsymbol{\nabla}V_{\rm e}\right)=-\iota(t)\delta(x)\delta(y)\delta(z), \tag{18}$$

where $\iota(t)$ is a monophasic pulse as depicted in Fig. 4 and is defined as

$$\iota(t)=\begin{cases}I_{\rm A}, & 0\le t<T_{\rm p}\\ 0, & T_{\rm p}\le t\le T_0\end{cases} \tag{19}$$

For the fiber bundle model oriented along the z-axis, equation (18) can be Fourier transformed in z and t to give a differential equation in $r=\sqrt{x^2+y^2}$. This can be solved to give an expression for the (z,t)-Fourier transformed extracellular potential [13]

$$\hat{V}_{\rm e}^{\rm fb}(x,y,k_z,w)=\frac{\hat{\iota}(w)}{4\pi\zeta_{\rm e,T}}\sqrt{\frac{2}{\pi}}K_0\big(\chi^{\rm fb}(k_z,w)r|k_z|\big), \tag{20}$$

where $\hat{\iota}(w)=\dfrac{1}{\sqrt{2\pi}}I_{\rm A}T_{\rm p}\mathrm{sinc}\left(\dfrac{wT_{\rm p}}{2}\right)$, K_0 is the zeroth order modified Bessel's function of the second kind and

$$\chi^{\rm fb}(k_z,w)=\sqrt{\frac{\zeta_{\rm e,L}(k_z,w)}{\zeta_{\rm e,T}}} \tag{21}$$

is a ratio measure of anisotropy between the longitudinal and transverse fiber directions. The expression in equation (20) can be used to reconstruct the solution in the space-time domain numerically via the inverse fast Fourier transform for (k_z,ω).

For the laminar tissue model, the extracellular potential can be found by Fourier transforming equation (18) in (x,y) and t, which results in

$$\zeta_{\rm e,T}\frac{\partial^2\hat{V}_{\rm e}^{\rm lm}}{\partial z^2}-\hat{\xi}_{{\rm e},r}^{\rm lm}k_r^2\hat{V}_{\rm e}^{\rm lm}=\frac{-\hat{\iota}(w)}{(2\pi)^{3/2}}\delta(z), \tag{22}$$

where $k_r=|\mathbf{k}_r|=|(k_x,k_y,0)|=\sqrt{k_x^2+k_y^2}$, and the admittivity in the radial direction defined via

$$\begin{aligned}\hat{\xi}_{{\rm e},r}^{\rm lm}k_r^2=&\int_{|\mathbf{u}|=1}\zeta_{\rm e,T}(k_r^2-(\mathbf{k}^T\mathbf{u})^2)d\mathbf{u}\\&+\int_{|\mathbf{u}|=1}\left(\frac{1}{\rho_{\rm i}}\frac{1+j\omega\tau_m+(\mathbf{k}^T\mathbf{u})^2\lambda_{0J}^2}{1+j\omega\tau_m+(\mathbf{k}^T\mathbf{u})^2\lambda_{0V}^2}\right)(\mathbf{k}^T\mathbf{u})^2d\mathbf{u}.\end{aligned} \tag{23}$$

The solution to this equation is detailed in Appendix C and is given as

$$\hat{V}_{\rm e}^{\rm lm}(\mathbf{k}_r,z,\omega)=\frac{-\hat{\iota}(w)}{(2\pi)^{3/2}\sqrt{\zeta_{\rm e,T}\hat{\xi}_{{\rm e},r}^{\rm lm}}k_r}\left(e^{-\chi^{\rm lm}(k_r,w)k_r|z|}\right), \tag{24}$$

where anisotropy ratio between direction within and transverse to the laminar plane is

$$\chi^{\rm lm}(k_r,w)=\sqrt{\frac{\hat{\xi}_{{\rm e},r}^{\rm lm}}{\zeta_{\rm e,T}}}. \tag{25}$$

Again, to obtain the spatiotemporal solution, equation (24) must be inverted using the inverse fast Fourier transform of (k_x,k_y) and w.

The solution for a point source stimulation for the isotropic tissue model is obtained once the integral over the distribution of orientations has been performed [29],

$$\hat{V}_{\rm e}^{\rm is}(\mathbf{k},w)=\frac{\hat{\iota}(w)}{(2\pi)^{3/2}\hat{\xi}_{\rm e}^{\rm is}}, \tag{26}$$

where $\hat{\xi}_{\rm e}^{\rm is}$ is the (isotropic) admittivity given in equation (30) of the results, which depends only on $K=|\mathbf{k}|=|(k_x,k_y,k_z)|=\sqrt{k_x^2+k_y^2+k_z^2}$ and w . As a consequence, we can perform a modified, one-dimensional, inverse Fourier transform of this equation with respect to K, instead of the normal three-dimensional inverse Fourier transform. The spatial form of the extracellular potential is given by

$$\hat{V}_{\rm e}^{\rm is}(R,w)=\frac{\mathcal{F}_K^{-1}\{-jK\hat{V}_{\rm e}^{\rm is}(K,w)\}}{R}, \tag{27}$$

where $R = |\mathbf{r}| = \sqrt{x^2+y^2+z^2}$ and $\mathcal{F}_K^{-1}$ denotes the (1-dimensional) inverse Fourier transform with respect to K (see also note [1]) Details of derivations to go from equation (26) to (27) is given in Appendix C 2.

III. RESULTS

Analytical and numerical results are presented in this section. First, we give the analytic expressions for admittivities of the three tissue models with different fiber orientation distributions in the Fourier domain. Second, approximate solutions of the extracellular potential for point source stimulation in the near-field and far-field regions for a laminar tissue are given. We finish the section by presenting numerical results on point source electrical stimulation of these tissue models. This illustrates (1) the effect of pulse width on changing the spatial profile of the extracellular potential and (2) the effect of distance from the electrode in altering electrical anisotropy in a tissue model that is nonetheless structurally homogeneous (the laminar model).

A. Admittivity Calculation

Expressions for the admittivity for three different tissue types were calculated based on the distribution of fiber orientations as defined in Section 2 of the Methods and illustrated in Fig. 3a. fiber bundle model, Fig. 3b. laminar model, and Fig. 3c. isotropic model. For the fiber bundle model, fibers are oriented in the z direction; for the laminar model, they are oriented in the xy plane; in the isotropic model, they are oriented in all directions.

Fiber bundle model

$$\begin{aligned}\hat{\xi}_{\mathrm{e,r}}^{\mathrm{fb}} =& \zeta_{\mathrm{e,T}},\\ \hat{\xi}_{\mathrm{e,z}}^{\mathrm{fb}}(\mathbf{k},w) =& \zeta_{\mathrm{e,L}}(k_z,w) = \frac{1+{\lambda_J}^2(w)k_z^2}{\rho_i(1+{\lambda_V}^2(w)k_z^2)}.\end{aligned} \tag{28}$$

Laminar model

$$\begin{aligned}\hat{\xi}_{\mathrm{e,z}}^{\mathrm{lm}} =& \zeta_{\mathrm{e,T}},\\ \hat{\xi}_{\mathrm{e,r}}^{\mathrm{lm}}(\mathbf{k},w) =& \frac{3\zeta_{\mathrm{e,T}}}{2} + \frac{1-\frac{{\lambda_{0J}}^2}{{\lambda_{0V}}^2}}{\rho_i{\lambda_V}^2(w)k_r^2}\\ &\times\left(1-\frac{1}{\sqrt{1+{\lambda_V}^2(w)k_r^2}}\right).\end{aligned} \tag{29}$$

Isotropic model

$$\begin{aligned}\hat{\xi}_{\mathrm{e}}^{\mathrm{is}}(\mathbf{k},w) =& \hat{\xi}_{\mathrm{e,r}}^{\mathrm{is}}(\mathbf{k},w) = \hat{\xi}_{\mathrm{e,z}}^{\mathrm{is}}(\mathbf{k},w) =\\ &\frac{4\zeta_{\mathrm{e,T}}}{3} + \frac{1}{\rho_i{\lambda_V}^2(w)K^2}\\ &\times\left(1-\frac{\tan^{-1}(K\lambda_V(w))}{K\lambda_V(w)}\right),\end{aligned} \tag{30}$$

where $\hat{\xi}_{\mathrm{e,r}}^{\mathrm{is}}(\mathbf{k},\omega)$ and $\hat{\xi}_{\mathrm{e,z}}^{\mathrm{is}}(\mathbf{k},\omega)$ are the admittivities in the r and z directions, respectively. ρ_i is the intracellular space resistivity. $\lambda_J(w)$ and $\lambda_V(w)$ are temporal frequency-dependent electrotonic length constants for current and voltage boundary conditions, which are defined as

$$\begin{aligned}\lambda_J(w) &= \frac{\lambda_{0J}}{\sqrt{1+jw\tau_m}},\\ \lambda_V(w) &= \frac{\lambda_{0V}}{\sqrt{1+jw\tau_m}}.\end{aligned} \tag{31}$$

Note that these length constants are complex numbers that have a phase as well as a magnitude. The temporal frequency dependence highlights the fact that the magnitudes of the length constants diminish as the temporal frequency increases. This is due to the lower impedance of the membrane capacitance at higher frequencies, thus reducing the path in the extracellular space that current must traverse before it can cross the membrane.

Fig. 5a. shows the full spatiotemporal frequency dependence of the admittivity using the isotropic model as an example. There is a transition from a low asymptotic magnitude for the admittivity to a high asymptotic magnitude as one moves from top-left to bottom right of the figure (high spatial frequency/low temporal frequency to low spatial frequency/high temporal frequency). This transition occurs in the region in which the frequency dependent electrotonic length constants are in commensurate with the applied spatial frequency, K (i.e., $K|\lambda_J(w)| \approx 1$ and $K|\lambda_V(w)| \approx 1$) (refer to Appendix C in [13] for a formal derivation of this relationship). Indicative frequency ranges for both intrinsic brain signals (EEG, LFP, and spikes) and electrical stimulation are marked, with intrinsic signals typically subject to a lower value of admittivity due to their low temporal frequency content relative to electrical stimulation. Intrinsic brain signals range from delta waves (0.5-4 Hz) up

[1] Note equation (27) involves a slight abuse of notation in which we have written the first functional argument of $\hat{V}_{\mathrm{e}}^{\mathrm{is}}$ as the $1-R$, the dimensional distance, when strictly it is the 3-dimensional point $\mathbf{r}$ whose distance from the origin is R. Similarly we have written the first argument of $\hat{V}_{\mathrm{e}}^{\mathrm{is}}$ as K, when it should be $\mathbf{k}$. This emphasizes that the dependence occurs only through the length of these vectors allowing a one- instead of three-dimensional inverse Fourier transform.

to spikes (1-2 kHz) in temporal frequency [22–24] , and from synapses ($\approx 1\mu$m, 10^6 cycle/m) to whole brain (≈ 0.1 m, 10 cycle/m)[23]. Electrical stimulation ranges from approximately 1 to 100 kHz in temporal frequency (pulse width 1 ms to 10 μs)[18–21], and spatial frequencies commensurate with size and spacing of electrodes, 10^2 to 10^5 cycle/m (≈ 1 cm to $\approx 10\mu$m)[25, 26].

Fig. 5b. compares the magnitude of the admittivity across the three different tissue models, as a function of spatial frequency. For components of the admittivity that are transverse to all fibers the curves are flat(i.e. for either $\hat{\xi}^{\mathrm{fb}}_{\mathrm{e,r}}$, aligned to a cylindrical radial direction, r for the fiber bundle model, or $\hat{\xi}^{\mathrm{lm}}_{\mathrm{e,z}}$, aligned to the z direction for the laminar model, and with no such direction for the isotropic model). This reflects the fact that the current (by definition) cannot pass along the inside of fibers, and instead is always forced to cross them through the extracellular space. For the admittivity in a direction parallel to any choice of fiber direction, the curves are sigmoidal; the magnitude goes from a high value at low spatial frequency to a low value at high spatial frequency. This is because the spatial frequencies higher than the scale of the electronic length constant have difficulty accessing the intracellular space along fibers. This second component of admittivity decreases as the tissue becomes more isotropic from fiber bundle, to laminar model, to isotropic model, particularly at lower spatial frequencies. This is due to the increased prevalence of fibers at crossed orientations in more isotropic models, which adds a component of the lower transverse admittivity to the higher longitudinal admittivity. Note the units are in terms of the inverse of the w-dependent electrotonic length constant for voltages boundary conditions, underscoring the fact that the temporal frequency dependence of the admittivity is mediated entirely through this constant in equations (28), (29) or (30).

B. Near-field and Far-field Approximations of Cellular Composite Model

The expressions for admittivity of the different models in equations (29)-(30), reach asymptotic limits of constant and pure conductivity in both the high and low spatial frequency limits. For a point source electrode, these limits correspond to the near-field and far-field approximations to the cellular composite model. The near- and far-field regions are determined by the electrotonic length constants; comparing the expressions in equation (31), we note that $|\lambda_V(\omega)| > |\lambda_J(\omega)|$. The near-field approximation describes the potential in the tissue close to the electrode $|\mathbf{r}| = R \ll |\lambda_J(\omega)|$, or alternatively, $K|\lambda_V(w)| \gg 1$ (see [13] Appendix C for an explanation of this equivalence). The far-field approximation is a good description of the potential at larger distances $R \gg |\lambda_V(\omega)|$, that is the case where $K|\lambda_J(w)| \ll 1$.

The near- and far-field limits are shown graphically in Fig. 6 for the isotropic model. For simplicity we considered a constant current input with an amplitude of 1μA to obtain a steady state solution. The cellular composite solution (green) interpolates between the near-field approximation close to the electrode (< 10 μm, blacked-dashed: analytical, magenta: numerical) and the far-field approximation distant from the electrode (> 300 μm, black-dotted: analytical, orange: numerical). In general, the analytical solution for near- or far-field approximations takes the classical form for a point source in an anisotropic volume conductor,

$$V_{\mathrm{e}}(\mathbf{r},t) = \frac{\iota(t)}{4\pi\sqrt{\sigma_r\sigma_z r^2 + \sigma_r^2 z^2}}, \tag{32}$$

where σ_r, σ_z are real constant conductivities in the r and z directions. These conductivities take different expressions depending on whether they apply in near- or far-field and depending on the model of fiber orientation, as shown in Table III. These expressions were obtained by taking the $K \to \infty$ or $K \to 0$ limits in equations (29)-(30) for near- and far-field approximations, respectively.

In Fig. 6, the magnitude of the near-field solution is an order of magnitude larger than the far-field counterpart for all values of electrode separation, R. This is due to the difference in conductivities, which can be understood physically by considering current paths in the tissue. Close to the electrode (near-field) most of the current is forced to pass through the comparatively narrow ($d \ll b$) extracellular space due to the very high impedance membrane, leading to low effective conductivity proportional to the effective extracellular conductivity, $\zeta_{\mathrm{e,T}}$. However, as the distance along the neurite increases, the current gradually distributes across the membrane over the scale of the (frequency-dependent) electrotonic length constant. At large distances, a majority of the current has accessed the comparatively wide-diameter intracellular space ($b \gg d$), leading to high effective conductivity dominated by the inverse of the intracellular resistivity (as $\dfrac{1}{\rho_{\mathrm{i}}} \gg \zeta_{\mathrm{e,T}}$).

C. Numerical Results

1. *Pulse Width Effect*

Fig. 7 compares the extracellular potentials of an isotropic neural tissue model for various monophasic pulse widths using two different frameworks for modeling electrical stimulation. The cellular composite framework has admittivity with the spatiotemporal frequency dependence of the isotropic model given in equation (30), while standard volume conductor framework corresponds to the near- and far-field approximations with conductivities given in the third row of Table III. The solutions to the cellular composite model for different pulse widths, denoted T_{p}, are all sketched in green, i.e., the

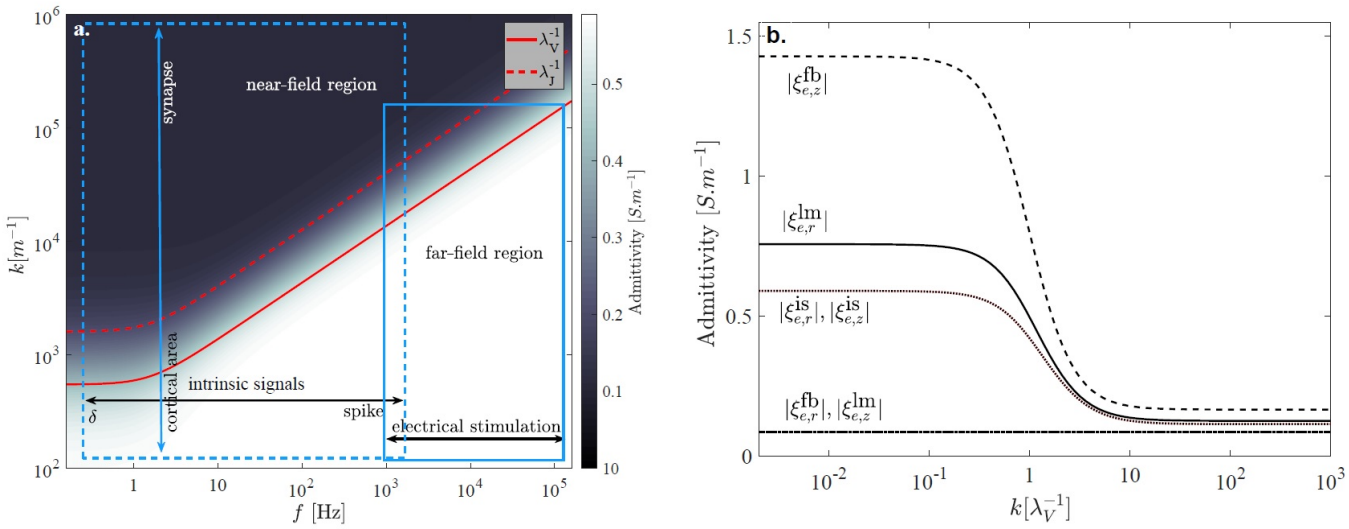

FIG. 5: (a) Admittivity magnitude as a function of spatial and temporal frequency for the isotropic model. Red curves indicate the inverse of the temporal frequency dependent electrotonic length constant given in equation (31) for voltage and current density boundary conditions (solid vs dotted lines respectively). Blue boxes indicate approximate spatiotemporal frequency ranges associated with intrinsic brain signal (dotted) and electrical stimulation (solid). The near-field region is the black region above the red-dotted line, while the far-field region is the white region below the red-solid line. The spatio-temporal frequency dependence of the admittivity of the fiber bundle and laminar models is not shown, but is qualitatively similar for admittivity in a direction parallel to any of their fibers. (b) Comparison of the magnitude of the admittivity as a function of the spatial frequency across three different tissue models: fiber bundle, laminar and isotropic (as marked). Sigmoidal curves indicated admittivity in any direction parallel with a fiber (regardless of orientation), while flat curves indicate admittivity in directions perpendicular to all fibers (fiber bundle, laminar models only, the same for both models). The spatial frequency k in this graph represents k_z, k_r, or K as appropriate for the different models, as per equation (28)-(30). Note that units of spatial frequency are in terms of the inverse of the electrotonic length constant for voltage, $\lambda_V(w)$, which contains the only temporal frequency dependence in the expressions for admittivity. Thus, the plots are valid for all temporal frequencies. All the cellular parameters (b, d, ρ, etc) are the same across the models. Refer to Table IV for the values.

TABLE III: Near-field and Far-field conductivities

Model	Near-field	Far-field
Fiber bundle	$\sigma_r^{\mathrm{bf}} = \zeta_{\mathrm{e,T}}$	$\sigma_r^{\mathrm{bf}} = \zeta_{\mathrm{e,T}}$
	$\sigma_z^{\mathrm{fb}} = 2\zeta_{\mathrm{e,T}}$	$\sigma_z^{\mathrm{fb}} = \dfrac{1}{\rho_i}$
Laminar model	$\sigma_r^{\mathrm{lm}} = \dfrac{3}{2}\zeta_{\mathrm{e,T}}$	$\sigma_r^{\mathrm{lm}} = \dfrac{\zeta_{\mathrm{e,T}}}{2} + \dfrac{1}{2\rho_i}$
	$\sigma_z^{\mathrm{lm}} = \zeta_{\mathrm{e,T}}$	$\sigma_z^{\mathrm{lm}} = \zeta_{\mathrm{e,T}}$
Isotropic model	$\sigma_r^{\mathrm{is}} = \dfrac{4}{3}\zeta_{\mathrm{e,T}}$	$\sigma_r^{\mathrm{is}} = \dfrac{4}{3}\zeta_{\mathrm{e,T}} + \dfrac{1}{3\rho_{\mathrm{i}}}$
	$\sigma_z^{\mathrm{is}} = \dfrac{4}{3}\zeta_{\mathrm{e,T}}$	$\sigma_z^{\mathrm{is}} = \dfrac{4}{3}\zeta_{\mathrm{e,T}} + \dfrac{1}{3\rho_{\mathrm{i}}}$

TABLE IV: Parameter values used in numerical calculations.

Parameter	b	d	ρ_{i}	ρ_{e}	R_{m}	τ_{m}
Value	0.5	0.03	0.7	0.7	1	1
Unit	μm	μm	$\Omega\cdot$m	$\Omega\cdot$m	$\Omega\cdot\mathrm{m}^2$	ms

light green for 10μs, the olive green for 100μs and the dark green for 1000μs. These solutions match the volume conductor solutions in the near- and far-field regions but also exhibit a transition between the two regions due to the spatiotemporal frequency dependence of the admittivity. This transition is pulse width-dependent, with the shorter pulse-width showing a transition closer to the electrode and a longer pulse width having a transition further from the electrode. The consequence is that a temporal parameter controlled by the user affects the spatial profile of the potential in the tissue. This coupled spatiotemporal filtering is a direct consequence of modeling the admittivity with a temporal and spatial frequency dependence, and is observed in all three models for directions that are parallel to at least some of the fibers in the tissue. These frequency dependencies

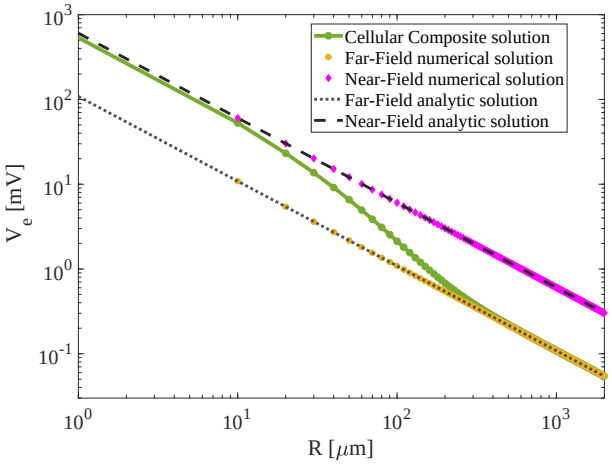

FIG. 6: Near-field and far-field limits to the point source solution to the cellular composite isotropic model. Green: Cellular composite numerical solution obtained by applying the inverse Fourier transform given by equation (27) to equation (26). Orange: Far-field approximation using the Taylor series expansion of equation (26) around $K = 0$ and numerically inverting the Fourier transform via equation (27). Black-dotted: The analytic solution for the far-field approximation from equation (32). Magenta: Near-field approximation from numerical inversion of the Fourier transform. This is the case when $K \to \infty$. Black-dashed: The analytic solution for the near-field approximation.

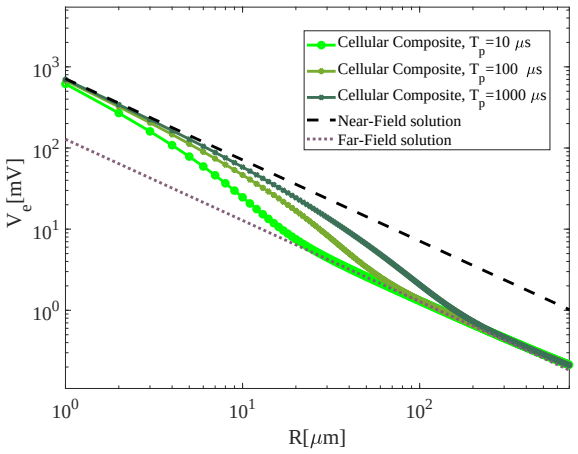

FIG. 7: Illustration of the pulse width effect on the transition of the extracellular potential from near- to far-field approximations. The point-source solution for the cellular composite model and isotropic structure is shown for three different monophasic rectangular pulse widths ($T_{\rm p} = 10, 100, 1000\mu$s, greens) relative to the near-field approximation (pink) and far-field approximation (black). The potential is sampled at the end of the pulse. Parameters are given in Table IV.

arise from the combination of the membrane capacitance (temporal frequency), and the different current pathways from the extracellular to the intracellular space (spatial frequency). The effect is mediated through dependence of the electrotonic length constant on the inverse of the square root of the temporal frequency in equation (31). This expression shows that shorter pulses, which contain higher spectral temporal frequencies, lead to shorter electronic length constants, enabling extracellular current to enter the neurite through the membrane on shorter spatial scales to access the intracellular pathway with higher effective conductivity.

2. *Anisotropy Effect*

To explain the effect of spatiotemporal filtering on anisotropy, we choose the neural tissue model with laminar structure where the fibers are only oriented in the (x, y) plane with no fiber along the z direction.

Fig. 8 shows that the degree of electrical anisotropy depends on separation from the point source electrode in the tissue, by plotting profiles of the extracellular potential in the (r, z) plane, where r is parallel to the plane and z is perpendicular. The four graphs (a)-(d) are sketched with different scales of resolution. Fig. 8a shows an area of up to 10 μm from the electrode. In this region, equipotentials for the cellular composite model (black) are close to circular, indicating that the potential profile is only weakly anisotropic at this distance compared to further out. This is confirmed by the close match to the equipotentials of the near-field approximation (white dashed), for which the ratio of conductivity in r vs z directions is given analytically to be $\sqrt{\frac{3\zeta_{\rm e,T}/2}{\zeta_{\rm e,T}}} \approx 1.2$. Physically, the weak degree of anisotropy is because all current is forced through the extracellular space in the near-field and the narrowness of this cross-section is only weakly dependent on direction.

As the distance from the electrode increases, around 10 times more, the equipotentials for the cellular composite and near-field solutions no longer coincide, as shown in Fig. 8b. However, the cellular composite solution is still only weakly anisotropic. In the range of 1000 μm from the electrode, shown in Fig. 8c., the effect of anisotropy becomes more pronounced, as shown by the pronounced long elliptical equipotentials with major axis oriented along the r-axis. The near-field solution has been replaced with the far-field solution to better display the change of behavior of the cellular composite model (black). This is the range where the cellular composite model makes a transition to match the far-field solution. By passing to the final range, in Fig. 8d., we see that the cellular composite and the far-field solutions are perfectly matched in a range of around 2000 μm from the electrode in the z direction and 4000 μm from the electrode in the r direction. For the far-field model the ratio

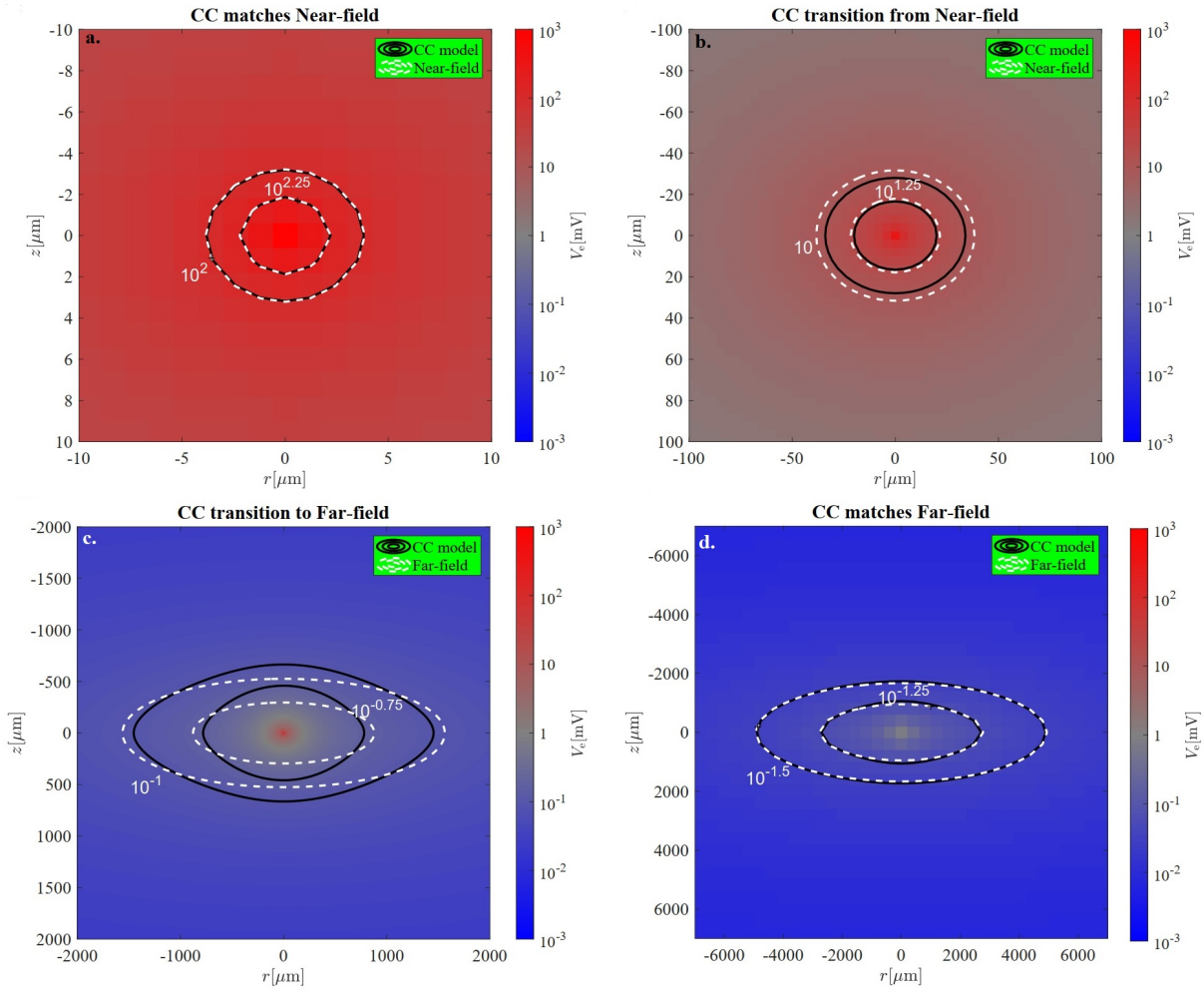

FIG. 8: Anisotropy effect. (a) Cellular composite contours (black) are matched with the near-field contours (white) for a pulse width of 100μs, in a range of less than 5 μm from the electrode. (b) Transition of the cellular composite solution from the near-field solution. (c) Transition of the cellular composite to the far-field in the range of less than 1000 μm from the electrode. (d) Cellular composite is matched with the anisotropic solution in the far-field region. The colorbar represents the logarithm of the extracellular potential in millivolts. Stimulation was with a rectangular monophasic pulse of 100 μs pulse-width and an amplitude of 1 μA is applied to the tissue.

of conductivity in r vs z directions is given analytically to be $\sqrt{\frac{1/2(\zeta_{e,T}+1/\rho_i)}{\zeta_{e,T}}} \approx 20$, if we use the parameters in Table IV. This is approximately 17 times more than the degree of anisotropy in the near-field region. Physically, this means that in the far-field region most current in the r direction (within a layer) enters the low impedance intracellular pathway via the membrane, with the effective conductivity of $1/2(\zeta_{e,T} + 1/\rho_i)$ (see TABLE III).

Note that the region of transition from weak to strong anisotropy is influenced by the pulse-width as well, via the temporal frequency dependence of the electrotonic length constants.

IV. DISCUSSION AND CONCLUSION

In this paper, we derived the electrical admittivity of a neural tissue model that accounts for cellular microstructure with various distributions for fiber orientations. We considered models with a uniform distribution of fiber orientation in one, two, or three dimensions (i.e., fiber bundle, laminar, or isotropic models). These may be considered as approximations to structures that are prevalent in the nervous system. For example, the retina and the neocortex have layered laminar structures [30, 31]. A more general model could incorporate a superposition of all three model types to capture the contribution of neurons/neurites with different morphologies in the same tissue. For example in neocortex, stellate morphologies could be approximated by a term akin to the isotropic

model, while pyramidal cells could be approximated by a combination of terms from the fiber bundle and laminar models, to capture the contribution of both ascending and lateral dendrites, respectively.

The key novel aspect of the derived electrical admittivity is its spatial and temporal frequency dependence. In general, this leads to spatiotemporal filtering of the extracellular potential. To illustrate the consequences of this we considered two effects. First, we investigated the effect of various pulse-widths on the extracellular potential of the tissue using the cellular composite and the standard volume conductor models. Due to the spatiotemporal frequency dependence of the admittivity, the spatial profile of the extracellular potential changed as the pulse width changed in the cellular composite model. The result showed longer transitions from the near-field to the far-field regions for longer pulse-widths. This is due to the temporal frequency dependent electrotonic length constants (equation (31)), which determine the distance along fibers over which current passes from the extracellular space to the intracellular space, via the membrane, to equilibrate the membrane potential to its resting value. Shorter pulses have more power at high frequencies in their spectrum, and thus shorter transition distances from near- to far-field. The near-field is characterized by relatively high effective resistivity because current is forced through the highly confined extracellular space. The far-field is characterized by lower effective resistivity due to the larger cross-sectional area of the fiber compared to the extracellular space. Between these two regimes, the complex-valued, temporal frequency dependent nature of the admittivity becomes pronounced. These effects of pulse width on the spatial profile of the extracellular potential cannot be addressed in the standard volume conductor model because in this approach neural tissue is described by a purely conductive element that is independent of temporal or spatial frequencies.

As a second example, numerical calculation illustrated how the degree of anisotropy in the electrical potential is influenced by separation from the electrode in the cellular composite model, despite the underlying structural homogeneity. The laminar model was used that has fibers running in the (x, y) plane but not in the z direction. This was contrasted with the solutions of the volume conductor models in the near-field and far-field regions where the degree of anisotropy of the extracellular potential was unaffected by separation from the electrode. Using a measure of anisotropy based on the ratio of the longitudinal to transverse admittivities, it was shown that the ratio is much smaller in the near-field compared to the far-field region for the cellular composite model. The behavior at distances more than the voltage electrotonic length constant was shown to be considerably more anisotropic. This is due to the current accessing the intracellular space in the far-field, but only in directions parallel to fibers.

These results were illustrated using a point source electrode. It is straight forward to include electrodes of finite size in the formalism if they have known surface current density (e.g. uniform density) by substituting the expression for that current density into the right hand side of equation (18) in place of the delta functions of x, y and z (see [32, 33] for an example with a disk electrode). In general, the inclusion of larger electrodes will not alter the qualitative conclusions of the two examples given here, which depend on a transition from near-field to the far-field in the extracellular potential. Physically the near-field occurs for distances from the electrode surface much less than the temporal frequency dependent electrotonic length constants, while the far-field occurs for distances from the surface much greater than electrotonic length constants, regardless of the electrode size. Quantitatively, the magnitude of the effects in the two examples reported here depend on the spatial distribution of the surface current density on the electrode and particularly its spatial Fourier transform. When there is significant power in this Fourier transform at spatial frequencies that span the range determined by the electronic length constants (i.e. above $1/\lambda_J(w)$ and below $1/\lambda_V(w)$), the effects reported here will be prominent. This is typically expected to be the case for even larger planar electrodes, because sufficiently high spatial frequencies in the distribution of source current density occur at both the edge of the electrode and in the direction perpendicular to its surface.

An important implication of these insights for neural implants is that the size and shape of the area of tissue activated by electrical stimulation could be controlled by stimulation parameters that are not normally considered to influence these outcomes of neural stimulation. Specifically, in the first example above, pulse width would influence the size of activated area, while in the second example, pulse amplitude would affect the shape (as well as size) of the activated area in anisotropic tissue (by changing the spatial range of activation). The size and shapes of activated areas are generally of key importance to the clinical applications of neural stimulation, e.g. affecting the size and shape of phosphenes in a retinal implant [4, 34]. Most electrodes used in clinical neuroprosthetic devices are sized in the range from 100s to 1000s of micrometers and use pulse widths from 10s to 1000s of microseconds. The present results suggest that size and shape of neural activity would be affected in such applications by the spatiotemporal frequency dependence of the tissue admittivity up to distances of a couple of hundred micrometers from the surface of the electrode. At distances beyond that, an appropriate, possibly anisotropic, volume conductor model coinciding with the far-field approximation would suffice.

The framework developed here for modeling neural tissue admittivity assumes a passive model for the electrical properties of the membrane (i.e. only resistive and capacitive impedance), which is also an assumption made in many modeling studies of neural stimulation [35]. Neural membranes also contain a variety of nonlinear voltage-dependent conductances that have been neglected in our

approach. Such nonlinear effects are difficult to treat mathematically. Changes in membrane conductance associated with the voltage-gated sodium and potassium conductances underlying action potential generation can be large compared to the passive conductance, but are also brief ($\approx$ 1 ms), are predominately found in the axons and somas rather dendrites and are typically asynchronous across the neural population during ongoing activity. These considerations suggest that activation of these conductances will be diffuse in time and space during ongoing activity, so that their contributions to the tissue admittivity are likely to be modest. During brief pulsatile electrical stimulation of neural tissue ($<$ 1 ms), membrane depolarization can be large, causing widespread, synchronous activation of sodium conductances, primarily in axons and soma. Any ensuing action potential usually occurs after the stimulation pulse because the regenerative process of full of sodium conductances activation takes longer (an additional 1-5 ms). The critical period determining how current from the electrode determines a spatial profile for the extracellular potential occurs during the pulse, when the sodium conductance are only partially activated. It is difficult to determine how much this level of sodium conductance activation will affect the overall tissue admittivity without a detailed simulation study of morphologically reconstructed neurons with Hodgkin-Huxley style dynamics. This is beyond the scope of the present study. However, any effect would decrease the membrane resistance, reduce electronic length constants, and thus shift the boundaries of the near- and far-field closer to the electrode. The qualitative effects described here are expected to remain. A second form of membrane conductance not considered explicitly here is the combined contribution of time-dependent synaptic conductances to the total membrane conductance. This can also be large *in vivo*, as a consequence of ongoing spontaneous activity [36]. In the framework developed here, this can be accounted for as a reduced effective passive membrane resistance determined by the mean rate of spontaneous activity of neurons in the tissue [37]. Once again this would shift the boundaries of the near- and far-field closer to the any source/sink/electrode.

A recent experimental study applying subretinal stimulation to the rat retina demonstrated an effect of pulse width on the spatial profile of activation of retinal ganglion cells analogous to the effect predicted here for extracellular potential (i.e. the first example effect)[38]. Stimulation with pulse widths increasing from 0.1 ms to 0.33 ms to 1 ms lead to progressively wider areas of activation, just as predicted here for the extracellular potential. This provides indirect evidence for the spatio-temporal frequency dependence of neural tissue admittivity. However, because the effect is observed at the level of neural activity rather than the extracellular potential, other factors such as a pulse duration-dependent threshold for the charge required to elicit a spike could also explain the results.

Experimental studies directly recording the extracellular potential are required to measure tissue admittivity. Using this approach, several experimental studies of the admittivity of neural tissue have examined whether it exhibits temporal frequency dependence, but have not considered the possibility of spatial frequency dependence as this is a novel concept in the literature on tissue impedance. The majority of studies have found only weak dependence of the admittivity on temporal frequency in the range 0.1 - 10 kHz [39–43], with the exception of the study of Gabriel et al. which found a much stronger dependence [44] (see Fig. 5 in [43] for a summary). While this range of frequencies is relevant to the temporal frequency dependence of the admittivity predicted here, most of these studies have considered spatial scales larger than a millimeter, which are only relevant to the far-field regime described here and for which there is expected to be little or no temporal frequency dependence in the admittivity (see Fig. 5a below 10^3 cycles/m). The exception is the study of Miceli et al [43] that used electrodes separated by 100μm and 125 μm. They also found weak temporal frequency dependence over the range 5-500 Hz, with a slightly higher increase in admittivity at the higher end of this range. This is in a spatio-temporal frequency region that once again does not provide a strong test of our predictions for tissue admittivity. It could nonetheless be consistent with our predictions, which show a similar increase in admittivity in the vicinity of 500 Hz at a spatial frequency of 10^4 cycles/m, which roughly corresponds to the 100μm spatial scale of their measurements (consider the appropriate cross-section across temporal frequency in the admittivity in Fig. 5). This increase corresponds to the border at which the admittivity begins increasing above its near-field limit. However, a definitive test of the spatiotemporal frequency-dependence of admittivity predicted here will require future experiments that measure across a greater range of spatial and temporal frequencies as covered in Fig. 5.

V. ACKNOWLEDGMENT

The authors would like to thank Idris D. Meffin for assistance in preparing schematic figures.

Appendix A: Derivation of Cellular Composite Model for Tissue Composed of Crossed Fibers via a Mean-Field Approximation

1. Fundamental Tissue Model

The fundamental tissue model described in section II A consists of tightly packed, interlocking neurites that partition the tissue into many elongated intracellular compartments and a single connected extracellular space that is highly confined and tortuous. Laplace's equa-

tion governs the spatial distribution of the intra- and extra-cellular potentials, ϕ_i and ϕ_e, respectively: $\boldsymbol{\nabla}^2\phi_c = 0, \quad c = \mathrm{i}, \mathrm{e}$. More fundamentally, the potentials are derived from a pair of equations consisting of a continuity equation for the current densities, $\boldsymbol{\Gamma}_\mathrm{i}$ and $\boldsymbol{\Gamma}_\mathrm{e}$, and a constitutive equation relating the current density to the potential,

$$\boldsymbol{\nabla} \cdot \boldsymbol{\Gamma}_c(\mathbf{r}, t) = 0, \tag{A1a}$$

$$\boldsymbol{\Gamma}_c(\mathbf{r}, t) \quad = -\rho_c^{-1}\boldsymbol{\nabla}\phi_c(\mathbf{r}, t), \tag{A1b}$$

where $\mathbf{r} = (x, y, z)$ is any point in the intracellular space if $c = \mathrm{i}$, or in the extracellular space if $c = \mathrm{e}$. ρ_i and ρ_e are the intracellular and extracellular resistivities, respectively.

The boundary conditions ensure continuity of current across the neural membrane and boundedness of the potential for all space and time:

$$\frac{1}{\rho_\mathrm{i}}\frac{\partial\phi_\mathrm{i}(\mathbf{r}, t)}{\partial n} = -J_\mathrm{m}(\mathbf{r}, t), \quad \forall \mathbf{r} \in \text{any membrane}, \tag{A2a}$$

$$\frac{1}{\rho_\mathrm{e}}\frac{\partial\phi_\mathrm{e}(\mathbf{r}, t)}{\partial n} = -J_\mathrm{m}(\mathbf{r}, t), \quad \forall \mathbf{r} \in \text{any membrane}, \tag{A2b}$$

$$|\phi_\mathrm{i}(\mathbf{r}, t)| \quad < \infty, \qquad \forall \mathbf{r} \in \text{any intracellular space}, \tag{A2c}$$

$$|\phi_\mathrm{e}(\mathbf{r}, t)| \quad < \infty \qquad \forall \mathbf{r} \in \text{the extracellular space}. \tag{A2d}$$

Here, $\frac{\partial}{\partial n}$ represents the derivative in the direction outwardly normal to the membrane surface. There may be other boundary conditions describing electrodes or insulating boundaries, that are unnecessary to consider here and are omitted. In addition, the current density through the membrane, J_m, is the sum of resistive and capacitive components. In the sub-threshold regime, in which the membrane behavior can be assumed to be linear and modeled by an RC-circuit, the relationship between the membrane current density and the membrane potential is given by

$$J_\mathrm{m} = C_\mathrm{m}\frac{dV_\mathrm{m}}{dt} + \frac{V_\mathrm{m}}{R_\mathrm{m}}, \tag{A3}$$

where

$$V_\mathrm{m}(\mathbf{r}, t) \triangleq \phi_\mathrm{i}(\mathbf{r}, t) - \phi_\mathrm{e}(\mathbf{r}, t), \quad \forall \mathbf{r} \in \text{a membrane}, \tag{A4}$$

and C_m and R_m are the specific membrane capacitance and specific passive membrane resistance, respectively.

2. Mean-field Derivation

To explicitly redefine the fundamental model in terms of a system of coupled NTES elements, we trivially rewrite equation (A1b) as a disjoint sum over NTES elements, with orientation defined by unit vector $\mathbf{u}$, and indexed within each orientation class by an integer n:

$$\boldsymbol{\Gamma}_c(\mathbf{r}, t) = \sum_{\mathbf{u},n} \boldsymbol{\Gamma}_c(\mathbf{r}, t)\mathbf{1}_{\mathbf{u},n}(\mathbf{r}). \tag{A5}$$

The function $\mathbf{1}_{\mathbf{u},n}(\mathbf{r})$ is the indicator function for the NTES element with orientation $\mathbf{u}$ and index n, which is 1 inside the NTES element and zero elsewhere, and thus serves to partition the space into sections occupied by each NTES element. On the outer NTES boundaries we define the extracellular potential and current density to be

$$V_\mathrm{e} \triangleq \phi_\mathrm{e}|_{\text{NTES boundary}}, \tag{A6a}$$

$$\mathbf{J}_\mathrm{e} \triangleq \boldsymbol{\Gamma}_\mathrm{e}|_{\text{NTES boundary}}. \tag{A6b}$$

To clarify, ϕ_e and $\boldsymbol{\Gamma}_\mathrm{e}$ are the potential and current density of the fundamental model, respectively, at any point in extracellular space while V_e and $\mathbf{J}_\mathrm{e}$ are the potential and current density (respectively) on the combined extracellular surface of all NTES elements. For each NTES element in isolation, the intra- and extracellular potentials, ϕ_i and ϕ_e, at any point inside the NTES obey the same set of partial differential equations and boundary conditions as described by equations (A1)-(A4). Additionally, in order for each NTES system to have a (unique) solution in isolation, ϕ_e must obey a boundary condition on the outer sheath of the NTES element, which can be stipulated in terms of either the extracellular potential or the extracellular current density:

$$\phi_\mathrm{e}(\mathbf{r}, t) \quad = V_\mathrm{e}(\mathbf{r}, t), \qquad \forall \mathbf{r} \in \text{outer NTES boundary}, \tag{A7a}$$

$$\frac{\partial\phi_\mathrm{e}(\mathbf{r}, t)}{\partial n} = -\rho_\mathrm{e}\mathbf{J}_\mathrm{e} \cdot \mathbf{n}(\mathbf{r}, t), \quad \forall \mathbf{r} \in \text{outer NTES boundary}. \tag{A7b}$$

Thus, we have a set of partial differential equations and boundary conditions for each NTES, which together form a system of partial differential equations and boundary conditions for the whole model of tissue. They are coupled together on the shared outer NTES boundaries via V_e and $\mathbf{J}_\mathrm{e}$, which must be found self-consistently.

Since we are ultimately only interested in deriving mean-field equations for the extracellular potential and current density, we can eliminate the dependence on intracellular and membrane currents and potentials in equations (A1)-(A4) but utilizing the concept of the electrical trans-impedance (or reciprocally, admittance) of an NTES element. The trans-impedance gives the relationship between spatiotemporal functions of current density and potential along the outer NTES boundary of the extracellular sheath:

$$(\mathbf{J}_\mathrm{e} \cdot \mathbf{n})(\mathbf{r}, t) = -\mathcal{T}_{\mathbf{u},n}[V_\mathrm{e}(\mathbf{r}, t)], \tag{A8}$$

where $\mathcal{T}_{\mathbf{u},n}$ is a linear operator representing the trans-impedance, acting on the potential over space and time

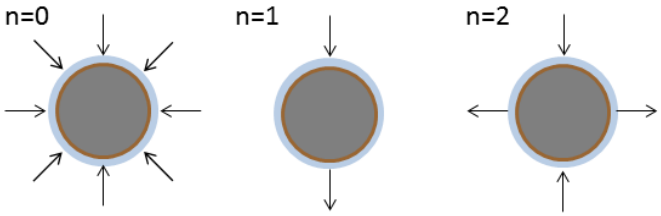

FIG. 9: Schematic showing the directions of current flow for the first three modes of the expansion of the expression for the trans-impedance of a cylindrical NTES element ($n = 0, 1, 2$). A cross-sectional view of the cylindrical NTES element is shown in each case, with the neurite membrane, intracellular space and extracellular space shown in brown, gray and blue-gray respectively. Current enters or leaves the NTES element along its outer boundary in directions shown by arrows. The $n = 0$ mode corresponds to current entering the boundary equally at all angles and then passing longitudinally along the inside of the NTES element. The $n = 1$ mode corresponds to current passing transversely from one side of the NTES element to the opposite side, entirely through the extracellular space. The $n = 2$ mode is also restricted to transverse current flow, but with a higher order symmetry in angular frequency such that current enters along one axis (e.g. vertical) and leaves via the perpendicular axis (e.g. horizontal). Higher order modes (not shown) are also transverse but with symmetries corresponding to higher angular frequencies.

for any position $\mathbf{r}$ on the boundary of NTES element, $\mathbf{u}, n$. That is, $\mathcal{T}_{\mathbf{u},n}$ gives the current density on the boundary for an arbitrary function of voltage applied along the boundary (voltage boundary condition), while $\mathcal{T}^{-1}_{\mathbf{u},n}$ gives the voltage on the boundary given an arbitrary function of current density applied along the boundary (current density boundary condition). The electrical trans-impedance completely characterizes electrical properties of an NTES element, including its internal structure of neurite membrane and intracellular space (via a fundamental theorem of impedance tomography, see [6] and references contained therein, especially section 4). It can be obtained by solving the system of PDEs for a NTES element given by equations (A1)-(A4) using either voltage or current density boundary conditions, given in equations (A6a) and (A6b), respectively. With the trans-impedance equation (A8) we obtain an alternative system of equations involving the extracellular quantities $\mathbf{J}_\mathrm{e}$ and $V_\mathrm{e}(\mathbf{r}, t)$ only, that applies on the combined extracellular boundary of NTES elements and must be solved self-consistently over adjoining NTES elements. On this boundary this system is identical to the original system comprising the constitutive equations (A1b), for the extracellular and intracellular space, together with the boundary conditions in equations (A2)-(A4).

We are now ready to make a series of simplifications and approximations to the fundamental tissue model to make it analytically tractable. The key simplification is to replace the irregular NTES elements with equivalent cylindrical elements.

(A1) We assume the trans-impedance of the irregularly shaped NTES elements is well approximated by that of cylindrical NTES elements.

This will be a reasonable approximation provided the two types of NTES elements share similar proportions (radius, extracellular sheath width) and electrical constants (intracellular and extracellular resistivity, specific membrane resistance and capacitance). We have previously derived expressions for the trans-impedance of a cylindrical NTES element in terms of cylindrical coordinates [16]. This involved an expansion of the potential and current density on the boundary, V_e and $\mathbf{J}_\mathrm{e}$, in terms of modes of the angular frequency $n = 0, 1, 2, \ldots$ of the cylindrical polar angle as shown in Fig. 9. The $n = 0$ mode corresponds to the longitudinal mode in which current passes along the fiber, including via the intracellular pathway by crossing the membrane, which is now hidden in equation (A8) (via algebraic elimination). The $n = 1$ mode corresponds to the simple traverse mode in which current passes across the fiber, entirely through the extracellular space. The $n = 2, 3, \ldots$ modes correspond to transverse modes with higher angular frequencies that are rarely observed in neural tissue.

(A2) We assume that only the $n = 0$ longitudinal and $n = 1$ transverse modes contribute to the bulk electrical properties of the tissue, so that the $n = 2, 3, \ldots$ modes can be neglected.

With this assumption it is possible to replace the cylindrical NTES element, which has an inhomogeneous internal structure comprising extra- and intracellular spaces, by an equivalent homogeneous cylindrical element (an hNTES element) occupying the same volume but with spatially uniform electrical admittivity such that the trans-impedances of the two elements are identical for the significant, i.e. first two, modes [12]. The linear trans-impedance operator in equation (A8) can then be described by the admittivity kernel, $\boldsymbol{\xi}_{\mathrm{e},\mathbf{u}}(\mathbf{r}, t)$, that is applied via convolution

$$\mathcal{T}_{\mathbf{u},n}[V_\mathrm{e}(\mathbf{r}, t)] = \frac{1}{2\pi}[\boldsymbol{\xi}_{\mathrm{e},\mathbf{u}}(\mathbf{r} - \mathbf{r}_{\mathbf{u},n}, t)] \underset{r_\mathbf{u},t}{*} [\boldsymbol{\nabla} V_\mathrm{e}(\mathbf{r}, t)] \quad \text{(A9)}$$

where $\mathbf{r}_{\mathbf{u},n}$ specifies the location of the centre of an hNTES element. For each fiber orientation, the position vector can be decomposed into coordinate directions parallel and perpendicular to the fiber $\mathbf{r} = (r_\mathbf{u}, \mathbf{r}_{\tilde{\mathbf{u}}})$ $(r_\mathbf{u} \in \mathbb{R}, \mathbf{r}_{\tilde{\mathbf{u}}} \in \mathbb{R}^2)$. The admittivity kernel involves a spatial convolution in the direction parallel to the fiber $r_\mathbf{u}$, as well as a temporal convolution, t (which together introduce the factor of $\frac{1}{2\pi}$). The Fourier transform of this admittivity kernel in three spatial and one temporal dimension is given by equations (8)-(10) for the fiber bundle. In the space-time domain the kernel has a more complicated form, which is given here for completeness,

though it is generally less useful

$$\boldsymbol{\xi}_{\mathrm{e},\mathbf{u}}(\mathbf{r},t)= \xi_{\mathrm{e,T}}\mathbf{I}_{3\times 3} + (\xi_{\mathrm{e,L}}(r_{\mathbf{u}},t) - \xi_{\mathrm{e,T}})\mathbf{u}\mathbf{u}^{T}, \quad \text{(A10)}$$

where

$$\xi_{\mathrm{e,T}}(r_{\mathbf{u}},t) = 2\pi\zeta_{\mathrm{e,T}}\delta(r_{\mathbf{u}})\delta(t) = \frac{2\pi d}{b\rho_{\mathrm{e}}}\delta(r_{\mathbf{u}})\delta(t), \quad \text{(A11a)}$$

$$\begin{aligned}\xi_{\mathrm{e,L}}(r_{\mathbf{u}},t) = {} & \frac{2\pi\delta(r_{\mathbf{u}})\delta(t)}{\rho_{\mathrm{i}}} \\ & - \frac{\sqrt{\pi}H(t)\tau_{\mathrm{m}}^{\frac{3}{2}}}{4\rho_{\mathrm{i}}\lambda_{0_{\mathrm{V}}}t^{\frac{5}{2}}}\left(\frac{2t}{\tau_{\mathrm{m}}} - \frac{r_{\mathbf{u}}^2}{\lambda_{0_{\mathrm{V}}}^2}\right)\times \\ & e^{-\left(\frac{t}{\tau_{\mathrm{m}}} + \frac{r_{\mathbf{u}}^2}{4\lambda_{0_{\mathrm{V}}}^2}\frac{\tau_{\mathrm{m}}}{t}\right)},\end{aligned} \quad \text{(A11b)}$$

In replacing the original internally inhomogeneous cylindrical NTES element, with an equivalent homogeneous cylindrical hNTES element, we perform a spatial smoothing of the original model on the spatial scale of the fiber diameter. Given the assumption above, this action leaves the extracellular current density and potential on the cylindrical NTES boundary unaltered, but in the interior of the cylinder it introduces smoothly interpolated versions, $\mathbf{J}_{\mathrm{e}}$ and V_{e} of the extracellular current density and potential (respectively) that arise from the spatially smoothed admittivity, as given in equations (8)-(10). This replaces the original interior description in terms of intra- and extracellular current densities and potentials, $\boldsymbol{\Gamma}_c$ and ϕ_c, $c = \mathrm{e}, \mathrm{i}$. The fundamental equation (A5) for the current density in this model becomes

$$\mathbf{J}_{\mathrm{e}}(\mathbf{r},t) = \sum_{\mathbf{u},n}\mathbf{J}_{\mathrm{e}}(\mathbf{r},t)\mathbf{1}_{\mathbf{u},n}(\mathbf{r}), \quad \text{(A12)}$$

$$= -\frac{1}{2\pi}\sum_{\mathbf{u},n}[\boldsymbol{\xi}_{\mathrm{e},\mathbf{u}}(\mathbf{r}-\mathbf{r}_{\mathbf{u},n},t)]\underset{r_{\mathbf{u}},t}{*}[\boldsymbol{\nabla}V_{\mathrm{e}}(\mathbf{r},t)]\mathbf{1}_{\mathbf{u},n}(\mathbf{r}), \quad \text{(A13)}$$

for $\mathbf{r}$ everywhere. Substituting the form of the admittivity kernel, equation (A10), for a cylindrical hNTES element into this equation (A12) we have

$$\begin{aligned}\mathbf{J}_{\mathrm{e}}(\mathbf{r},t) = {} & -\zeta_{\mathrm{e,T}}\mathbf{I}_{3\times 3}\boldsymbol{\nabla}V_{\mathrm{e}}(\mathbf{r},t) \\ & - \sum_{\mathbf{u},n}[(\xi_{\mathrm{e,L}}(r_{\mathbf{u}},t) - \xi_{\mathrm{e,T}})\mathbf{u}\mathbf{u}^{T}]\underset{r_{\mathbf{u}},t}{*}[\boldsymbol{\nabla}V_{\mathrm{e}}(r_{\mathbf{u}},\mathbf{r}_{\tilde{\mathbf{u}}},t)] \\ & \times \frac{\mathbf{1}_{\mathbf{u},n}(\mathbf{r})}{2\pi}\end{aligned} \quad \text{(A14)}$$

The first term in this equation is a transverse component derived from equation (A10) that is same for all fiber orientations. Consequently the sum over disjoint hNTES elements from equation (A12) merges to give a single homogeneous and isotropic contribution to the current density. It is resistive (i.e. no spatial or temporal frequency dependence) and describes the local flow of current around fibers purely in the extracellular space (i.e. without any "hidden" pathways through the intracellular space). The terms in the sum are the longitudinal components of each fibre and retain the convolutional form in $(r_{\mathbf{u}},t)$ that includes the flow of current between distant extracellular points on the fiber via the "hidden" intracellular and transmembrane pathways.

The next issue concerns the coupling of cylindrical hNTES elements. In the original fundamental model, NTES elements were coupled via extracellular current flow across their complicated and irregular shared outer boundaries. For cylindrical hNTES elements it is not geometrically possible to construct arrangements of ideal cylinders without any gaps between them. Instead we extend further the mean-field approximation by taking advantage of the aspects of the reformulated model to consider a situation in which fiber arrangements with both gaps and overlaps are allowed. There a several considerations that make this a reasonable approximation. First, spatially overlapping fibers are still coupled via the passage of current through the extracellular space, as they should be, despite have their interiors intersecting, because the reformulated model uses extracellular variables only (current density and potential). Second, current can still flow across gaps between fibers due to the presence of the first term, admittivity component in equation (A14) that applies equally everywhere in space (i.e. no gaps) and describes the local current flow around fibers purely through the extracellular space. In general this is the correct form of local coupling of fibers because any current leaving an hNTES element will be forced to pass locally through the extracellular space in this manner until it reaches another hNTES element of the appropriate orientation where it may be absorbed according to the longitudinal mode of current flow, as described by the terms in the sum in equation A14. This is because the part of the longitudinal current that accesses the low resistance intracellular pathway must do so over a length scale greater than the electronic length constant. Consequently flow of current varying on spatial scales smaller than the electronic length constant of a fiber occurs purely through the extracellular pathways. Consequently,

(A3) We assume that the average separation between fibers of similar orientation in the tissue is less than the electronic length constant.

Although the length constant is dependent on the temporal frequency of stimulation, it is generally in the order of hundreds of micrometers and greater than 10 μm even when stimulation pulses have spectral peaked at high stimulation frequencies of 100 kHz, making this a reasonable assumption.

With the forgoing arguments we can rewrite equation (A14) without regard to whether hNTES elements intersect or leave gaps, assuming only an average density of fibers of each orientation, such that the combined volume of hNTES elements completely fills the tissue vol-

ume.

$$\mathbf{J}_{\mathrm{e}}(\mathbf{r},t) = -\zeta_{\mathrm{e,T}}\mathbf{I}_{3\times3}\boldsymbol{\nabla}V_{\mathrm{e}}(\mathbf{r},t) - \sum_{\mathbf{u},n}[(\xi_{\mathrm{e,L}}(r_{\mathbf{u}},t)-\xi_{\mathrm{e,T}})\mathbf{u}\mathbf{u}^T]\underset{r_{\mathbf{u}},t}{*}\boldsymbol{\nabla}[V_{\mathrm{e}}(r_{\mathbf{u}},\mathbf{r}_{\check{\mathbf{u}}},t)] \times \frac{c_b(\mathbf{r}_{\check{\mathbf{u}}}-\mathbf{r}_{\check{\mathbf{u}},n})}{2\pi}. \tag{A15}$$

where $c_b(\mathbf{r}_{\check{\mathbf{u}}}-\mathbf{r}_{\check{\mathbf{u}},n})$ is the circ function centred at fiber location $\mathbf{r}_{\check{\mathbf{u}},n}$, which is 1 inside the radius of the hNTES element and 0 outside, and replaces the indicator function for that element. Taking the Fourier transform of the equation (A15) in three spatial and one temporal dimension we can write

$$\hat{\hat{\mathbf{J}}}_{\mathrm{e}}(\mathbf{k},\mathbf{w}) = -\zeta_{\mathrm{e,T}}\mathbf{I}_{3\times3}\boldsymbol{\nabla}\hat{\hat{V}}_{\mathrm{e}}(\mathbf{k},w) - \frac{1}{2\pi}\sum_{\mathbf{u},n}(\hat{\hat{\xi}}_{\mathrm{e,L}}(k_{\mathbf{u}},w)-\hat{\hat{\xi}}_{\mathrm{e,T}})\mathbf{u}\mathbf{u}^T \times [\check{\mathbf{c}}_b(\mathbf{k}_{\check{\mathbf{u}}})e^{-j\mathbf{k}_{\check{\mathbf{u}}}^T\mathbf{r}_{\check{\mathbf{u}},n}}]\underset{\mathbf{k}_{\check{\mathbf{u}}}}{*}[j\mathbf{k}\hat{\hat{V}}_{\mathrm{e}}(k_{\mathbf{u}},\mathbf{k}_{\check{\mathbf{u}}},w)] \tag{A16}$$

$$= -\zeta_{\mathrm{e,T}}\mathbf{I}_{3\times3}\boldsymbol{\nabla}\hat{\hat{V}}_{\mathrm{e}}(\mathbf{k},w) - \frac{1}{2\pi}\sum_{\mathbf{u}}jk_{\mathbf{u}}(\hat{\hat{\xi}}_{\mathrm{e,L}}(k_{\mathbf{u}},w)-\hat{\hat{\xi}}_{\mathrm{e,T}})\mathbf{u} \times [\check{\mathbf{c}}_b(\mathbf{k}_{\check{\mathbf{u}}})\sum_n e^{-j\mathbf{k}_{\check{\mathbf{u}}}^T\mathbf{r}_{\check{\mathbf{u}},n}}]\underset{\mathbf{k}_{\check{\mathbf{u}}}}{*}[\hat{\hat{V}}_{\mathrm{e}}(k_{\mathbf{u}},\mathbf{k}_{\check{\mathbf{u}}},w)]. \tag{A17}$$

where, in the first line the convolution in $(r_{\mathbf{u}},t)$ becomes a product of functions in $(k_{\mathbf{u}},w)$, while the product of functions in $\mathbf{r}_{\check{\mathbf{u}}}$ becomes a convolution over $\mathbf{k}_{\check{\mathbf{u}}}$. To ease mathematical complexity we assume that fibers of orientation, $\mathbf{u}$, are evenly distributed on a square grid with separation $d_{\mathbf{u}}$, which allows us to write the sum over hNTES elements with this orientation as a Dirac comb $\sum_n \exp(-j\mathbf{k}_{\check{\mathbf{u}}}^T\mathbf{r}_{\check{\mathbf{u}},n}) = (2\pi)^2/d_{\mathbf{u}}^2\sum_{\mathbf{n}}\delta(\mathbf{k}_{\check{\mathbf{u}}}-\mathbf{n}/d_{\mathbf{u}})$ where $\mathbf{n}=(n_1,n_2)\in\mathbb{Z}^2$ indexes the square grid. The convolution in equation (A16) may then be performed giving

$$\hat{\hat{\mathbf{J}}}_{\mathrm{e}}(\mathbf{k},w) = -\zeta_{\mathrm{e,T}}\mathbf{I}_{3\times3}\boldsymbol{\nabla}\hat{\hat{V}}_{\mathrm{e}}(\mathbf{k},w) - 2\pi\sum_{\mathbf{u}}jk_{\mathbf{u}}(\hat{\hat{\xi}}_{\mathrm{e,L}}(k_{\mathbf{u}},w)-\hat{\hat{\xi}}_{\mathrm{e,T}})\mathbf{u} \times \frac{1}{d_{\mathbf{u}}^2}\sum_{\mathbf{n}}\check{\mathbf{c}}_b\left(\frac{|\mathbf{n}|}{d_{\mathbf{u}}}\right)\hat{V}_{\mathrm{e}}(k_{\mathbf{u}},\mathbf{k}_{\check{\mathbf{u}}}-\mathbf{n}/d_{\mathbf{u}},w). \tag{A18}$$

The $\mathbf{n}=\mathbf{0}$ term in the sum of the above equation gives $\frac{(b_{\mathbf{u}})^2}{2d_{\mathbf{u}}^2}\hat{\hat{V}}_{\mathrm{e}}(k_{\mathbf{u}},\mathbf{k}_{\check{\mathbf{u}}},w)$ using that $\check{\mathbf{c}}_b(\mathbf{0})=b_{\mathbf{u}}^2/2$. The remaining higher order terms in the sum sample $\hat{\hat{V}}_{\mathrm{e}}(\mathbf{k},w)$ at spatial frequencies greater than or equal to the frequency of the fiber spacing in the tissue (of given orientation $\mathbf{u}$). This analysis concerning the contributions of the different spatial frequencies to the current density will continue to hold if we relax the square-grid arrangement of fiber, to allow fibers that are distributed more randomly in the tissue, but with the same density. Consequently,

(A4) We assume that the total contribution of the electrical potential/field at spatial frequencies finer than the spacing of fibers with similar orientation makes a negligible contribution to the current density at spatial frequencies larger than the spacing of fibers with similar orientation.

The expression for the current density then becomes

$$\hat{\hat{\mathbf{J}}}_{\mathrm{e}}(\mathbf{k},w) = -\int\left(\zeta_{\mathrm{e,T}}\mathbf{I}_{3\times3}+(\hat{\hat{\xi}}_{\mathrm{e,L}}(k_{\mathbf{u}},w)-\hat{\hat{\xi}}_{\mathrm{e,T}})\mathbf{u}\mathbf{u}^T\right) \times \check{\boldsymbol{\nabla}}\hat{\hat{V}}_{\mathrm{e}}(\mathbf{k},w)P(\mathbf{u})\,d\mathbf{u}. \tag{A19}$$

where the density of hNTES elements with orientation $\mathbf{u}$ is $P(\mathbf{u})=\pi b_{\mathbf{u}}^2/d_{\mathbf{u}}^2$, and, in the limit of a continuous distribution of fiber orientations, the sum over $\mathbf{u}$ becomes an integral. This gives the mean-field approximation for the current density given by equations (12) & (13). This can be interpreted as a mean-field approximation for the admittivity given by the average over the orientations of hNTES elements as given in equation (14).

Appendix B: Admittivity Calculation for Laminar Structure

For a laminar structure with infinitely many fibers, the admittivity can be computed in the Fourier domain from equation (14),

$$\hat{\hat{\boldsymbol{\xi}}}_{\mathrm{e}}^{\mathrm{lm}} = \int_{|\mathbf{u}|=\mathbf{1}}P(\mathbf{u})\hat{\hat{\boldsymbol{\xi}}}_{\mathrm{e},\mathbf{u}}(\mathbf{k},w)d\mathbf{u} = \frac{1}{2\pi}\int_{|\mathbf{u}|=\mathbf{1}}\hat{\hat{\xi}}_{\mathrm{e,T}}(I_{3\times3}-\mathbf{u}\mathbf{u}^T)d\mathbf{u} + \frac{1}{2\pi}\int_{|\mathbf{u}|=\mathbf{1}}\left(\frac{1}{\rho_{\mathrm{i}}}\frac{1+jw\tau_m+(\mathbf{k}^T\mathbf{u})^2\lambda_{0J}^2}{1+jw\tau_m+(\mathbf{k}^T\mathbf{u})^2\lambda_{0V}^2}\mathbf{u}\mathbf{u}^T d\mathbf{u}\right), \tag{B1}$$

where we have substituted the expression in equation (8) for the admittivity of a fibers with orientation $\mathbf{u}=[\cos\theta,\sin\theta,0]^T$. The solutions to these integrals can be obtained by converting the integral over $\mathbf{u}$ to an integral over θ and have a form

$$\hat{\hat{\boldsymbol{\xi}}}_{\mathrm{e}}^{\mathrm{lm}} = \begin{bmatrix}\hat{\hat{\boldsymbol{\xi}}}_{\mathrm{e},r}^{\mathrm{lm}} & 0\\ 0 & \hat{\hat{\boldsymbol{\xi}}}_{\mathrm{e},z}^{\mathrm{lm}}\end{bmatrix}, \tag{B2}$$

where $\hat{\hat{\boldsymbol{\xi}}}^{\rm lm}_{{\rm e},r}$ is a 2×2 block matrix describing the admittivity in the r-direction

$$\hat{\hat{\boldsymbol{\xi}}}^{\rm lm}_{\rm e,r} = \left(\frac{1}{2}\hat{\hat{\xi}}_{\rm e,T} + \frac{1}{2\rho_i}\frac{\lambda^2_{0J}}{\lambda^2_{0V}} - \frac{1}{\rho_i}\frac{(1-\frac{\lambda^2_{0J}}{\lambda^2_{0V}})f(k_r)}{\lambda^2_V(w)k_r^2\sqrt{1+\lambda^2_V(w)k_r^2}}\right) \times \begin{bmatrix}1 & 0\\ 0 & 1\end{bmatrix} + \frac{1}{\rho_i}\frac{(1-\frac{\lambda^2_{0J}}{\lambda^2_{0V}})f^2(k_r)}{\lambda^2_V(w)k_r^4\sqrt{1+\lambda^2_V(w)k_r^2}}\begin{bmatrix}k_y^2 & -k_xk_y\\ -k_xk_y & k_x^2\end{bmatrix} \tag{B3}$$

in which $f(k_r) = 1-\sqrt{1+\lambda^2_V(w)k_r^2}$. The second diagonal element in equation (B2) is the admittivity in the z direction, as per equation (29), and is given by

$$\hat{\hat{\xi}}^{\rm lm}_{{\rm e},z} = \hat{\hat{\xi}}_{\rm e,T}. \tag{B4}$$

Although there is no fiber oriented in the z direction, this admittivity is the result of stacking planar tissues on top of each other in a homogeneous medium. The factor in front of the 2x2 identity matrix in equation (B3) corresponds to the admittivity in the r direction (as per equation (29). The second matrix term turns out to be physically irrelevant as the following argument shows. By analyzing equation (B2) and calculating the eigenvalues (s_1, s_2) and eigenvectors ($\mathbf{v}_1$, bfv_2) of the second matrix on the right hand side of equation (B3), we find

$$\begin{aligned} s_1 =& 0, \quad \mathbf{v}_1 = [k_x, k_y]^T,\\ s_2 =& k_r^2, \quad \mathbf{v}_2 = [k_y, -k_x]^T. \end{aligned} \tag{B5}$$

The first of these eigenvectors is proportional to the radial components of $\check{\boldsymbol{\nabla}} = j[k_x, k_y]$ that appears in the constitutive equation (7) for cellular composite model. Since the physical meaning of the admittivity is defined by the constitutive equation, so the admittivity always appears pre-multiplying $\check{\boldsymbol{\nabla}}$ in any physically meaningful mathematical expression. Consequently, the first eigenvector gives no contribution as its eigenvalue is zero, while second eigenvector is physically irrelevant, as it is orthogonal to $\check{\nabla}$, and so contributes nothing in the constitutive equation.

As an aside, a check on the correctness of equation (B3) is that it should have an invariant form under rotation in the r-plane. This is true if and only if

$$\hat{\hat{\boldsymbol{\xi}}}^{\rm lm}_{\rm e,r}(\mathbf{k}_r, w) = \boldsymbol{R}\hat{\hat{\boldsymbol{\xi}}}^{\rm lm}_{\rm e,r}(\boldsymbol{R}\mathbf{k}_r, w)\boldsymbol{R}^T, \tag{B6}$$

where $\boldsymbol{R} = \begin{bmatrix}\cos\theta & -\sin\theta\\ \sin\theta & \cos\theta\end{bmatrix}$ is the rotation matrix. It can be checked that the sub-matrix $\hat{\hat{\boldsymbol{\xi}}}^{\rm lm}_{\rm e,r}$ is rotationally invariant.

Appendix C: Extracellular Potential Calculation

1. Laminar Model

To simplify the calculations, a two-dimensional Fourier transform in (x, y) and a one-dimensional in time are applied to both sides of equation (18),

$$\check{\boldsymbol{\nabla}}^T \int_{|\mathbf{u}|=\mathbf{1}} \hat{\hat{\boldsymbol{\xi}}}_{\rm e,\mathbf{u}} d\mathbf{u}\check{\boldsymbol{\nabla}}\check{V}_{\rm e} = \frac{-\hat{\imath}(w)}{2\pi\sqrt{2\pi}}\delta(z), \tag{C1}$$

where $\check{\boldsymbol{\nabla}} = [jk_x, jk_y, \frac{\partial}{\partial z}]$. Replacing $\hat{\hat{\boldsymbol{\xi}}}_{\rm e,\mathbf{u}}$ with the definition in equation (8) and arranging different terms, an ordinary differential equation in z is given,

$$\hat{\hat{\xi}}_{\rm e,T}\frac{\partial^2\hat{\hat{V}}^{\rm lm}_{\rm e}}{\partial z^2} - \hat{\hat{\xi}}^{\rm lm}_{{\rm e},r}k_r^2\hat{\hat{V}}^{\rm lm}_{\rm e} = \frac{-\hat{\imath}(w)}{(2\pi)^{3/2}}\delta(z), \tag{C2}$$

where $k_r = \sqrt{k_x^2+k_y^2}$, and

$$\begin{aligned}\hat{\hat{\xi}}^{\rm lm}_{{\rm e},r}k_r^2 =& \int_{|\mathbf{u}|=\mathbf{1}} \hat{\hat{\xi}}_{\rm e,T}(k_r^2 - (\mathbf{k}^T\mathbf{u})^2)\frac{d\mathbf{u}}{2\pi}\\ &+ \int_{|\mathbf{u}|=\mathbf{1}} \left(\frac{1}{\rho_{\rm i}}\frac{1+j\omega\tau_m+(\mathbf{k}^T\mathbf{u})^2\lambda^2_{0J}}{1+j\omega\tau_m+(\mathbf{k}^T\mathbf{u})^2\lambda^2_{0V}}\right)(\mathbf{k}^T\mathbf{u})^2\frac{d\mathbf{u}}{2\pi},\end{aligned} \tag{C3}$$

in which the unit vector $\mathbf{u} = [\cos\theta, \sin\theta, 0]^T$ gives the fiber orientation.

The integral over the orientation in equation (C3) can be performed by choosing a coordinate system in θ such that $\mathbf{k}^T\mathbf{u} = k_r\cos\theta$ to give the analytical solutions

$$\begin{aligned}\hat{\hat{\xi}}^{\rm lm}_{{\rm e},r}k_r^2 =& \left(\frac{1}{2}\hat{\hat{\xi}}_{\rm e,T} + \frac{1}{2\rho_i}\frac{\lambda^2_{0J}}{\lambda^2_{0V}}\right)k_r^2\\ &+ \frac{1}{\rho_i}\frac{(1-\frac{\lambda^2_{0J}}{\lambda^2_{0V}})}{\lambda_V(w)^2}\left(1-\frac{1}{\sqrt{1+\lambda_V(w)^2k_r^2}}\right).\end{aligned} \tag{C4}$$

Subsequently, the solution to the second order differential equation (C2) with constant coefficients is calculated as

$$\begin{aligned}\hat{\hat{V}}_{\rm e}(\mathbf{k}_r, w, z) =& \frac{-\hat{\imath}(w)}{(2\pi)^{3/2}\sqrt{\zeta_{{\rm e},T}\hat{\hat{\xi}}_{{\rm e},r}}k_r}\Big(e^{\chi^{\rm lm}(k_r,w)z}\\ &- e^{\chi^{\rm lm}(k_r,w)z}\Big)H(z)\\ &+ A_1e^{\chi^{\rm lm}(k_r,w)z} + A_2e^{-\chi^{\rm lm}(k_r,w)z},\end{aligned} \tag{C5}$$

where

$$\chi^{\rm lm}(k_r, w) = \sqrt{\frac{\hat{\hat{\xi}}^{\rm lm}_{{\rm e},r}}{\zeta_{{\rm e},T}}} \tag{C6}$$

is a measure of anisotropy, $H(z)$ is the Heaviside step function, and A_1 and A_2 are to be found through the

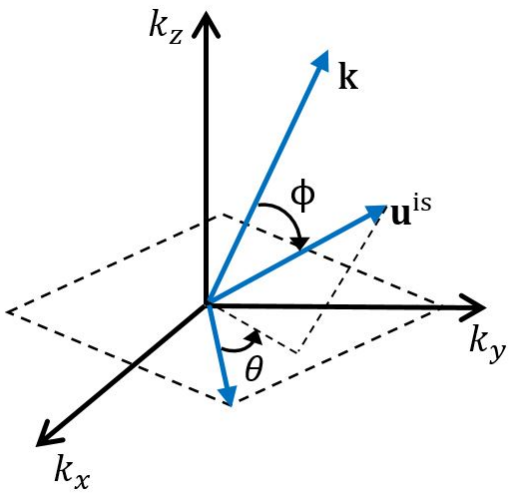

FIG. 10: A modified spherical coordinate system aligned to the direction of the fiber, $\mathbf{u}^{\text{is}}$, such that $\mathbf{k}$ makes polar angle ϕ, and azimuthal angle θ with $\mathbf{u}^{\text{is}}$. The original Cartesian coordinate system in (k_x, k_y, k_z) is shown for reference.

choice of boundary conditions. As it is assumed that the fibers are infinitely long, the voltage at infinity; i.e., $\lim_{z\to\pm\infty} \hat{V}_{\text{e}} < \infty$, should be finite. Given equation (C5), to satisfy the condition at $z \to \infty$, we choose $k_1 = \hat{\imath}(w)/(2\pi)^{3/2}\sqrt{\zeta_{\text{e},T}\hat{\xi}_{\text{e},r}}k_r$. To have a finite potential when $z \to -\infty$, $k_2 = 0$. Therefore, equation (C5) is simplified to

$$\hat{V}_{\text{e}}(\mathbf{k}_r, w, z) = \frac{-\hat{\imath}(w)}{(2\pi)^{3/2}\sqrt{\zeta_{\text{e},T}\hat{\xi}_{\text{e},r}}k_r}\left(e^{-\chi(k_r,w)|z|}\right). \quad \text{(C7)}$$

This is the Fourier domain extracellular potential of tissue with a laminar structure, which needs to be inverted numerically.

2. Isotropic Model

To obtain equation (26), we resort to equation (18) and this time apply a four-dimensional Fourier transform to both sides of this equation that gives

$$\hat{\hat{V}}_{\text{e}}^{\text{is}}(\mathbf{k}, w) = \frac{\hat{\imath}(w)}{(2\pi)^{3/2}\mathbf{k}^{\mathbf{T}}\left(\int_{|\mathbf{u}|=\mathbf{1}} P(\mathbf{u})\boldsymbol{\xi}_{\text{e},\mathbf{u}}d\mathbf{u}\right)\mathbf{k}}, \quad \text{(C8)}$$

where $\hat{\hat{V}}_{\text{e}}^{\text{is}}$ shows the Fourier transform of the extracellular potential calculated in Cartesian coordinates and $P(\mathbf{u}) = P(\theta, \phi) = \sin\phi/4\pi$ as explained in equation (26). The parameterization of this integral in spherical polar coordinates results in

$$\frac{1}{4\pi}\int_0^{2\pi}\int_0^{\pi}\mathbf{k}^T\left(\hat{\xi}_{\text{e,T}}\mathbf{I}_{3\times3} + (\hat{\boldsymbol{\xi}}_{\text{e,L}}(\mathbf{k}, w|\mathbf{u}^{\text{is}}) - \hat{\xi}_{\text{e,T}})\mathbf{u}^{\text{is}}\mathbf{u}^{\text{is}^T}\right) \times \mathbf{k}\sin\phi\; d\phi\; d\theta. \quad \text{(C9)}$$

We choose the spherical polar coordinate system such that axis of rotation is aligned with the vector $\mathbf{k}$. Thus, ϕ is the angle between $\mathbf{k}$ and the unit vector $\mathbf{u}^{\text{is}}$, so that $\mathbf{k}^T\mathbf{u}^{\text{is}} = K\cos\phi$. The angle θ is the angle between projection of $\mathbf{u}^{\text{is}}$ onto the plane perpendicular to $\mathbf{k}$, and some arbitrary vector in that plane (polar angle). This choice of coordinates allows a one-dimensional inverse Fourier transform rather than a three-dimensional inverse Fourier transform as explained in [29]. This is due to the fact that the result of the calculation in equation (C9) is only dependent on $K = |\mathbf{k}|$. The following calculation is then required to go from a Cartesian to a Spherical coordinates and obtain equation (27)

$$\begin{aligned}
\hat{V}_{\text{e}}^{\text{is}}(|R|, w) =& \frac{1}{(2\pi)^{(3/2)}}\iiint \hat{\hat{V}}_{\text{e}}^{\text{is}}(\mathbf{k}, w)\times \\
& e^{j(k_x,k_y,k_z).(x,y,z)}dk_xdk_ydk_z, \\
=& \frac{1}{(2\pi)^{(3/2)}}\iiint \hat{\hat{V}}_{\text{e}}^{\text{is}}(\mathbf{k}, w)\times \\
& e^{jKR\cos\phi}K^2\sin\phi\; dKd\theta d\phi, \\
=& \frac{1}{(2\pi)^{(1/2)}}\int_0^{\infty}\int_0^{\pi}\hat{\hat{V}}_{\text{e}}^{\text{is}}(\mathbf{k}, w)K^2\times \\
& e^{jKR\cos\phi}\sin\phi\; dKd\phi, \\
=& \frac{1}{(2\pi)^{(1/2)}}\int_0^{\infty} -\frac{1}{jKR}\hat{\hat{V}}_{\text{e}}^{\text{is}}(\mathbf{k}, w)K^2\times \\
& (e^{-jKR} - e^{jKR})\; dK, \\
=& \frac{1}{(2\pi)^{(1/2)}}\int_{-\infty}^{\infty} -\frac{jK}{R}\hat{\hat{V}}_{\text{e}}^{\text{is}}(\mathbf{k}, w)e^{jKR}\; dK
\end{aligned} \quad \text{(C10)}$$

If $1/R$ is factored out so that the remaining expression is the definition of an inverse Fourier transform of $\mathcal{F}_K^{-1}\{-jK\hat{\hat{V}}_{\text{e}}^{\text{is}}(K, w)\}$. Hence,

$$\hat{V}_{\text{e}}^{\text{is}}(R, w) = \frac{\mathcal{F}_K^{-1}\{-jK\hat{\hat{V}}_{\text{e}}^{\text{is}}(K, w)\}}{R}. \quad \text{(C11)}$$

Appendix D: Extension to Spherically Projected Gaussian Distribution of Fibers in a Plane

In realistic tissue, fibers are not necessarily oriented uniformly. This means fibers in a specific direction may

outnumber fibers in other directions. To account for this fact in laminar tissue we assume different standard deviations in the x and y directions. Based on this assumption, a corresponding orientation distribution function $P(\mathbf{u})$, and hence the extracellular potential are calculated.

The spherically projected Gaussian distribution in two-dimension with polar angle θ is given by

$$P_p(\theta) = \frac{\eta}{\pi(\cos^2\theta + \eta^2 \sin^2\theta)}. \tag{D1}$$

where η is a parameter describing the degree of anisotropy that can be derived from a two-dimensional Gaussian distribution in (x, y). The Gaussian distribution can be expressed as

$$P(x,y) = \frac{1}{2\pi\gamma_x\gamma_y} e^{\left(-\frac{x^2}{2\gamma_x^2} - \frac{y^2}{2\gamma_y^2}\right)}, \tag{D2}$$

where γ_x and γ_y are the standard deviations in the x and y directions, respectively.

To capture different orientations of fibers, this function is transformed into a polar coordinates by choosing $x = r\cos\theta$ and $y = r\sin\theta$

$$P(r,\theta) = \frac{1}{2\pi\gamma_x\gamma_y} e^{r^2\left(-\frac{\cos\theta^2}{2\gamma_x^2} - \frac{\sin\theta^2}{2\gamma_y^2}\right)}. \tag{D3}$$

This function is then projected onto a circle around the origin to remove the dependency on the fiber distances from the origin. This can be done by performing integration over r from zero to infinity

$$P_p(\theta) = \frac{\eta}{\pi(\cos^2\theta + \eta^2 \sin^2\theta)}, \tag{D4}$$

where $\eta = \dfrac{\gamma_x}{\gamma_y}$. The calculation of admittivity is very similar to the case of uniform distribution of fibers in equation (C2) with $\hat{\hat{\boldsymbol{\xi}}}^{\mathrm{lm}}_{\mathrm{e},r} k_r^2$ replaced by

$$\begin{aligned}\hat{\hat{\boldsymbol{\xi}}}^{\mathrm{lm}}_{\mathrm{e},xy} k_r^2 = &\int_\theta \frac{\eta \hat{\hat{\xi}}_{\mathrm{e},T}}{\pi(\cos^2\theta + \eta^2\sin^2\theta)}(K^2 - (\mathbf{k}^T\mathbf{u})^2)d\theta \\ &+ \int_\theta \frac{\eta}{\pi\rho_i(\cos^2\theta + \eta^2\sin^2\theta)} \frac{1 + \lambda_J^2(\mathbf{k}^T\mathbf{u})^2}{1 + \lambda_V^2(\mathbf{k}^T\mathbf{u})^2} d\theta.\end{aligned} \tag{D5}$$

Solving these integrals using Maple or Mathematica, we obtain

$$\begin{aligned}\hat{\hat{\boldsymbol{\xi}}}^{\mathrm{lm}}_{\mathrm{e},r} k_r^2 =& \xi_{\mathrm{e,T}} \frac{k_x^2 + \eta k_y^2}{1+\eta} + \frac{\lambda_{0J}^2}{\lambda_{0V}^2} \frac{\eta k_x^2 + k_y^2}{\rho_i(1+\eta)} + \frac{(1 - \frac{\lambda_{0J}^2}{\lambda_{0V}^2})}{\rho_i \lambda_V^2} \\ &\times \left(1 - \frac{\eta\Big(\eta\lambda_V^2\left(f(\eta)\left(k_x^2 - k_y^2\right) + \lambda_V^2 k_r^2\left(\eta^2 k_x^2 + k_y^2\right)\right)\Big)}{D} \right. \\ &\left. + \frac{\eta\Big(f(\eta)\left(\eta^2 - 1 + \lambda_V^2\left(\eta^2 k_x^2 - k_y^2\right)\right)\sqrt{1 + \lambda_V^2 k_r^2}\Big)}{D} \right),\end{aligned} \tag{D6}$$

where $f(\eta) = \eta^2 - 1$ and

$$\begin{aligned}D =& \sqrt{1 + \lambda_V^2 k_r^2}\Big[f(\eta)^2 + 2f(\eta)\lambda_V^2\left(\eta^2 k_x^2 - k_y^2\right) \\ &+ \lambda_V^4\left(\eta^2 k_x^2 + k_y^2\right)^2\Big].\end{aligned} \tag{D7}$$

Note that for brevity, the argument w is dropped from $\lambda_J(w)$ and $\lambda_V(w)$ in the above equations. According to these equations, one can choose appropriate distribution proportion, η, to obtain the extracellular potential solution in the Fourier domain. In a special case of $\eta = 1$, equation (C4) is recovered. The extracellular potential in the case of Gaussian distribution of fiber orientation is also of the form of equation (C7). This equation needs to be inverted numerically to obtain the extracellular potential.

[1] G. H. Baltuch and M. B. Stern. *Deep brain stimulation for Parkinson's disease*. CRC Press, 2007.

[2] G. Clark. *Cochlear implants: fundamentals and applications*. Springer Science and Business Media, 2006.

[3] J. Tombran-Tink, C.J. Barnstable, and J.F. Rizzo. *Visual prosthesis and ophthalmic devices: New hope in sight*. Springer Science and Business Media, 2007.

[4] A.E. Hadjinicolaou, H. Meffin, M.I. Maturana, S.L. Cloherty, and M.R. Ibbotson. Prosthetic vision: Devices, patient outcomes and retinal research. *Clinical and Experimental Optometry*, 98(5):395–410, 2015.

[5] P.G. Patil and D.A. Turner. The development of brain-machine interface neuroprosthetic devices. *Neurotherapeutics*, 5(1):137–146, 2008.

[6] L. Borcea. Electrical impedance tomography. *Inverse problems*, 18(6):R99, 2002.

[7] G.T. Einevoll, Ch. Kayser, N.K. Logothetis, and S. Panzeri. Modelling and analysis of local field potentials for studying the function of cortical circuits. *Nature Reviews. Neuroscience*, 14(11):770, 2013.

[8] K.H. Pettersen, A. Devor, I. Ulbert, A.M. Dale, and G.T. Einevoll. Current-source density estimation based on inversion of electrostatic forward solution: effects of finite extent of neuronal activity and conductivity discontinuities. *Journal of Neuroscience Methods*, 154(1):116–133, 2006.

[9] G.T. Einevoll, K.H. Pettersen, A. Devor, I. Ulbert, E. Halgren, and A.M. Dale. Laminar population analysis: estimating firing rates and evoked synaptic activity from multielectrode recordings in rat barrel cortex. *Jour-*

nal of Neurophysiology, 97(3):2174–2190, 2007.

[10] E. Syková and Ch. Nicholson. Diffusion in brain extracellular space. *Physiological Reviews*, 88(4):1277–1340, 2008.

[11] A. Lehmenkühler, E. Syková, J. Svoboda, K. Zilles, and Ch. Nicholson. Extracellular space parameters in the rat neocortex and subcortical white matter during postnatal development determined by diffusion analysis. *Neuroscience*, 55(2):339–351, 1993.

[12] H. Meffin, B. Tahayori, E. Sergeev, I.M.Y. Mareels, D.B. Grayden, and A.N. Burkitt. Modelling extracellular electrical stimulation: III. derivation and interpretation of neural tissue equations. *Journal of Neural Engineering*, 11(6):065004, 2014.

[13] B. Tahayori, H. Meffin, E. Sergeev, I. Mareels, A.N. Burkitt, and D.B. Grayden. Modelling extracellular electrical stimulation: IV. effect of the cellular composition of neural tissue on its spatio-temporal filtering properties. *Journal of Neural Engineering*, 11(6):065005, 2014.

[14] W.R. Holmes. Cable equation. *Encyclopedia of Computational Neuroscience*, pages 471–482, 2015.

[15] H. Meffin and T. Kameneva. The electrotonic length constant: a theoretical estimate for neuroprosthetic electrical stimulation. *Biomedical Signal Processing and Control*, 6(2):105–111, 2011.

[16] H. Meffin, B. Tahayori, D.B. Grayden, and A.N. Burkitt. Modeling extracellular electrical stimulation: I. Derivation and interpretation of neurite equations. *Journal of Neural Engineering*, 9(6):065005, 2012.

[17] B. Tahayori, H. Meffin, S. Dokos, A.N. Burkitt, and D.B. Grayden. Modeling extracellular electrical stimulation: II. Computational validation and numerical results. *Journal of Neural Engineering*, 9(6):065006, 2012.

[18] L.N. Ayton, P.J. Blamey, R.H. Guymer, C.D. Luu, D.A. Nayagam, N.C. Sinclair, M.N. Shivdasani, J. Yeoh, M.F. McCombe, R.J. Briggs, et al. First-in-human trial of a novel suprachoroidal retinal prosthesis. *PloS One*, 9(12):e115239, 2014.

[19] C.M. McKay and H.J. McDermott. The perceptual effects of current pulse duration in electrical stimulation of the auditory nerve. *The Journal of the Acoustical Society of America*, 106(2):998–1009, 1999.

[20] E. Moro, R.J.A. Esselink, J. Xie, M. Hommel, A.L. Benabid, and P. Pollak. The impact on parkinson's disease of electrical parameter settings in stn stimulation. *Neurology*, 59(5):706–713, 2002.

[21] R. Fisher, V. Salanova, Th. Witt, R. Worth, Th. Henry, R. Gross, K. Oommen, I. Osorio, J. Nazzaro, D. Labar, et al. Electrical stimulation of the anterior nucleus of thalamus for treatment of refractory epilepsy. *Epilepsia*, 51(5):899–908, 2010.

[22] J.W. Britton, L.C. Frey, J.L. Hopp, P. Korb, M.Z. Koubeissi, W.E. Lievens, E.M. Pestana-Knight, and E.K.L. St. *Electroencephalography (EEG): An introductory text and atlas of normal and abnormal findings in adults, children, and infants*. American Epilepsy Society, Chicago, 2016.

[23] E.R. Kandel, J.H. Schwartz, T.M. Jessell, et al. *Principles of neural science*, volume 5. McGraw-Hill New York, 2013.

[24] G. Buzsáki, C.A. Anastassiou, and C. Koch. The origin of extracellular fields and currents – EEG, ECoG, LFP and spikes. *Nature Reviews Neuroscience*, 13(6):407, 2012.

[25] M. Radivojevic, D. Jäckel, M. Altermatt, J. Müller, V. Viswam, A. Hierlemann, and D.J. Bakkum. Electrical identification and selective microstimulation of neuronal compartments based on features of extracellular action potentials. *Scientific Reports*, 6:31332, 2016.

[26] D.R. Freestone, L. Kuhlmann, D.B. Grayden, A.N. Burkitt, A. Lai, T.S. Nelson, S. Vogrin, M. Murphy, W. D'Souza, R. Badawy, et al. Electrical probing of cortical excitability in patients with epilepsy. *Epilepsy & Behavior*, 22:S110–S118, 2011.

[27] D.R. McNeal. Analysis of a model for excitation of myelinated nerve. *Biomedical Engineering, IEEE Transactions on*, (4):329–337, 1976.

[28] F. Rattay. Analysis of models for external stimulation of axons. *Biomedical Engineering, IEEE Transactions on*, (10):974–977, 1986.

[29] O. Monfared, D. Nešić, D.R. Freestone, D.B. Grayden, B. Tahayori, and H. Meffin. Electrical stimulation of neural tissue modeled as a cellular composite: Point source electrode in an isotropic tissue. In *Engineering in Medicine and Biology Society (EMBC), 36th Annual International Conference of the IEEE*, pages 4856–4859. IEEE, 2014.

[30] H. Wässle. Parallel processing in the mammalian retina. *Nature Reviews Neuroscience*, 5(10):747, 2004.

[31] V. Braitenberg and A. Schüz. *Anatomy of the cortex: statistics and geometry*, volume 18. Springer Science & Business Media, 2013.

[32] T. Esler, R.R. Kerr, B. Tahayori, D.B. Grayden, H. Meffin, and A.N. Burkitt. Minimizing activation of overlying axons with epiretinal stimulation: The role of fiber orientation and electrode configuration. *PLoS One*.

[33] T. Esler, M. Maturana, R.R. Kerr, D.B. Grayden, A.N. Burkitt, and H. Meffin. Biophysical basis of the linear electrical receptive fields of retinal ganglion cells. *Journal of Neural Engineering*.

[34] J.D. Weiland, A.K. Cho, and M.S. Humayun. Retinal prostheses: current clinical results and future needs. *Ophthalmology*, 118(11):2227–2237, 2011.

[35] E.N. Warman, W.M. Grill, and D. Durand. Modeling the effects of electric fields on nerve fibers: determination of excitation thresholds. *IEEE Transactions on Biomedical Engineering*, 39(12):1244–1254, 1992.

[36] D. Paré, E. Shink, H. Gaudreau, A. Destexhe, and E.J. Lang. Impact of spontaneous synaptic activity on the resting properties of cat neocortical pyramidal neurons in vivo. *Journal of Neurophysiology*, 79(3):1450–1460, 1998.

[37] H. Meffin, A.N. Burkitt, , and D.B. Grayden. An analytical model for the 'large, fluctuating synaptic conductance state' typical of neocortical neurons in vivo. *Journal of Computational Neuroscience*, 16(2):159–176, 2004.

[38] W. Tong, M. Stamp, N. Apollo, K. Ganesan, H. Meffin, S. Prawer, and M.R. Garrett, D.J. Ibbotson. Improved visual acuity using a retinal implant and an optimized stimulation strategy. *Journal of Neural Engineering*, Accepted:doi.org/10.1088/1741–2552/ab5299, 2019.

[39] J.B. Ranck. Specific impedance of rabbit cerebral cortex. *Experimental Neurology*, 7:144–152, 1963.

[40] N.K. Logothetis, Ch. Kayser, and A. Oeltermann. In vivo measurement of cortical impedance spectrum in monkeys: implications for signal propagation. *Neuron*, 55(5):809–823, 2007.

[41] M. Elbohouty. *Electrical conductivity of brain cortex slices in seizing and non-seizing states*. Hamilton, New

Zealand: University of Waikato., 2013.

[42] T. Wagner, U. Eden, J. Rushmore, Ch.J. Russo, L. Dipietro, F. Fregni, S. Simon, S. Rotman, N.B. Pitskel, C. Ramos-Estebanez, et al. Impact of brain tissue filtering on neurostimulation fields: a modeling study. *Neuroimage*, 85:1048–1057, 2014.

[43] S. Miceli, T.V. Ness, G.T. Einevoll, and D. Schubert. Impedance spectrum in cortical tissue: Implications for propagation of LFP signals on the microscopic level. *eNeuro*, 4(1):e0291, 2017.

[44] S. Gabriel, R. Lau, and C. Gabriel. The dielectric properties of biological tissues: II. Measurements in the frequency range 10 Hz to 20 GHz. *Physics in Medicine & Biology*, 41(11):2251, 1996.